High-temperature magnetic order and coexisting spin dynamics in $PrCu_2$: Manifestations of multipolar effects

A. Schenck and F. N. Gygax
Institute for Particle Physics of ETH Zürich (IPP), 5232 Villigen PSI, Switzerland

Y. Ōnuki
Faculty of Science, Osaka University, Machikaneyama, Toyonaka, Osaka 560, Japan

(Received 29 April 2003; published 19 September 2003)

We present a comprehensive muon-spin-rotation/relaxation (μSR) study of the high-temperature magnetic order ($T_N \simeq 65$ K) in $PrCu_2$, first observed quite unexpectedly in 1998 [A. Schenck *et al.*, Phys. Rev. B **58**, 5205 (1998)]. Measurements in zero and longitudinal fields as a function of temperature, orientation of the single-crystal sample, and strength of applied magnetic field H_{ext} confirmed the previous findings and allowed us to determine the properties of the internal spontaneous fields $\boldsymbol{B}$ in detail. It is found that $\boldsymbol{B}$ is strictly confined to the crystallographic (a,c) plane and encloses on average an angle θ of $30° - 45°$ with the a axis, depending on temperature. Both $|\boldsymbol{B}|$ and θ display a large variation. This is consistent with, but does not unambiguously prove, the incommensurately modulated antiferromagnetic structure observed below ~ 50 mK by neutron scattering [S. Kawarazaki and J. Arthur, J. Phys. Soc. Jpn. **57**, 1077 (1988)]. The estimated ordered electronic moment of $\sim 0.29\ \mu_B$ is smaller than the value quoted by Kawarazaki *et al.* ($0.54\ \mu_B$). The temperature dependence of $|\boldsymbol{B}|$ is highly unusual and scales perfectly with the temperature dependence of the elastic constant C_{66} [R. Settai *et al.*, J. Phys. Soc. Jpn **67**, 636 (1998)], implying that the ordered moment is proportional to the strain susceptibility involving the O_{xy} quadrupole moment. μ^+ is also found to be exposed to fluctuating field components inducing spin-lattice relaxation. The relaxation rate λ consists of a field-independent but rather anisotropic term and an essentially isotropic but field-dependent term. The first term reflects the Jahn-Teller transition at 7.5 K by a cusplike anomaly. Transverse-field measurements at 6 kOe and above 100 K allowed us to determine the anisotropic Knight shift, or the dipolar coupling tensor, from which it follows that μ^+ are located at $4e$ sites. At lower temperatures, we find evidence that the contact-hyperfine coupling constant becomes temperature and orientation dependent.

DOI: 10.1103/PhysRevB.68.104422 PACS number(s): 75.25.+z, 76.75.+i, 76.60.Es, 76.60.Jx

I. INTRODUCTION

Since 1972 it has been known that the orthorhombic singlet-ground-state compound $PrCu_2$ develops below 50 mK a cooperative nuclear-electronic antiferromagnetic order.[1] This conclusion was drawn from magnetic susceptibility and specific-heat measurements. The latter also indicated that below 1 K any ordered moment cannot be larger than 4.5% of the full Pr^{3+} moment ($3.38\mu_B$). Fifteen years went by before this ultralow temperature order was confirmed directly in a neutron-scattering experiment.[2] Polarization and intensity analysis showed that below 50 mK the nuclear and electronic moments are sinusoidally modulated in magnitude with a propagation vector $\boldsymbol{k}=(0.24,0,068)$ and that the moments are aligned nearly parallel to the crystallographic a axis. The total saturated moment was determined to be $0.31\mu_B$ and the electronic part of it to $0.54\mu_B$. The intensity of the diffraction peaks vanished at 50 mK and no hint of a persisting magnetic order above that temperature was evident. Hence it was a real surprise when 10 years later zero-field μSR measurements[3] revealed a persisting magnetic order up by more than *three orders of magnitude* above the previous transition temperature, which appeared to be consistent with the incommensurate order of Ref. 2. Criticism was raised that this might be a muon-induced effect, but we will argue that this cannot be the case. In this work, we will present comprehensive μSR measurements in zero, longitudinal, and transverse field (ZF, LF, TF), which confirm our earlier results and allow us to characterize the magnetic order in much detail. Also the identification of the μ^+ site in $PrCu_2$ is reported.

Historically the interest in $PrCu_2$ derives from another observation, namely the occurrence of a cooperative Jahn-Teller distortion at $T_{JT} \simeq 7.5$ K, first identified in 1974 (Ref. 4) and following years,[5,6] and believed to be driven by quadrupolar ordering. More recently (1995), the detection of a metamagnetic transition in $PrCu_2$ (Ref. 7) has started a flurry of further investigations involving magnetization, magnetostriction, magnetoresistance, and de Haas–van Alphen measurements.[8] The metamagnetic transition was seen up to at least 50 K, above which temperature the required field must have exceeded the available maximum of ~ 380 kOe or it started to be absent.[9] Also the cooperative Jahn-Teller transition was studied in more detail via thermal expansion,[10,11] specific heat, elastic constants, and magnetization measurements as a function of an external field H_{ext}.[10] The latter studies allowed us to derive the highly anisotropic phase diagram of the Jahn-Teller transition. Of particular interest is the strong temperature dependence of the elastic constant C_{66} which, as we will see, appears to govern also the behavior of the spontaneous internal field revealed by the μSR measurements below ~ 65 K. Both the metamagnetic and

 ©2003 The American Physical Society

the Jahn-Teller transition features could be quantitatively explained on the basis of the crystalline-electric-field (CEF) Hamiltonian, acting on the $^3H_4$ ground-state multiplet of Pr^{3+},[9,12] and quadrupole-quadrupole interaction terms, i.e., $K_{JT}\langle O_{xy}\rangle O_{xy}$, responsible for the ferroquadrupolar order below T_{JT}, and $K_M\langle O_2^2\rangle O_2^2$, which switches its sign from negative to positive across the metamagnetic transition as a result of a rotation of the quadrupole moment O_2^2.[8,11]

So far no connection has been made between the magnetic order below 50–60 mK and the higher-temperature quadrupolar-interaction-driven phenomena. The present results, on the other hand, suggest that the high-temperature magnetic order is intimately connected to quadrupolar effects. Since our observations show that the high-temperature magnetic order extends unchanged down to 20 mK, the question arises as to what is really happening below 50–60 mK. We suggest that the phase transition seen at 50–60 mK concerns only the Pr nuclear-spin system, and that the persisting electronic order may have escaped detection (see also the discussion in Ref. 1).

The paper is organized as follows. In Sec. II, we will present experimental details. Section III deals with the ZF and LF measurements. A large portion is devoted to the analysis of the ZF signals and their orientation dependence, making full use of the availability of spectra in the forward/ backward, up/ down, and right directions with respect to the μ^+ beam momentum. The possibility to use different initial μ^+ spin polarizations ranging from being parallel to the beam momentum to being turned by $\sim 45°$ towards the vertical direction is also exploited. This analysis will allow us to extract the direction of the spontaneous internal fields relative to the crystal frame. The information is complemented by data obtained in LF. This procedure has never before been applied to this extent and the outcome is another demonstration of the power of μSR in studying magnetic structures even in complicated cases. Section IV is devoted to the transverse-field measurements, allowing the identification of the location of the implanted μ^+. In Sec. V, we compare calculated field distributions, using the incommensurate magnetic structure of Ref. 2, with the experimental findings and arrive at excellent fits. We further discuss the observed spin-lattice relaxation results and the temperature dependence of the spontaneous average internal fields and arrive at the conclusion that the magnetic order is probably induced by quadrupolar effects. The paper concludes with a summary in Sec. VI.

II. EXPERIMENTAL DETAILS

The μSR measurements were performed at the Swiss Muon Source of PSI using various spectrometers: the general purpose instrument (GPS) and the low-temperature instrument (LTF) on the $\pi M3$ beam line, the Dolly instrument on the $\pi E3$ and $\pi E1$ beam lines ($\pi M3$, $\pi E1$ and $\pi E3$ provide surface μ^+ with essentially 100% spin polarization and 4 MeV kinetic energy), and the general purpose spectrometer (GPD) on the decay beam line μE1.

The LTF allows us to apply temperatures between ~ 20 mK and a few Kelvin, while the other instruments allow us to apply temperatures between 1.8 K and room temperature. External fields up to 6 kOe can be applied parallel to the incoming μ^+ in the GPS and Dolly spectrometers and up to 5 kOe perpendicular to the incoming μ^+ in the GPD. The latter instrument was used in the TF measurements to be able to apply the external field parallel to the *a* axis which was not possible in the other instruments. Since the $\pi M3$ beam line is equipped with a spin rotator, the μ^+ polarization $\boldsymbol{P}_\mu(0)$ can be rotated up to $\sim 50°$, from nearly parallel to the beam axis towards the vertical (up) direction. Since the spin rotator is also used as a positron separator, the initial μ^+ polarization is never strictly parallel to the beam axis but is rotated away by a minimum angle of $\sim 12°$. The $\pi E1$ and $\pi E3$ beam lines were at the time of the measurements not equipped with a spin rotator (but a positron separator), and here the initial μ^+ polarization was practically parallel to the beam axis. Both GPS and Dolly allow one to monitor the decay positrons from the implanted μ^+ in five positron detectors placed in forward (F)/ backward (B), up (U)/ down (D), and right (R) directions with respect to the μ^+ beam momentum, as shown in the schematic arrangement in Fig.

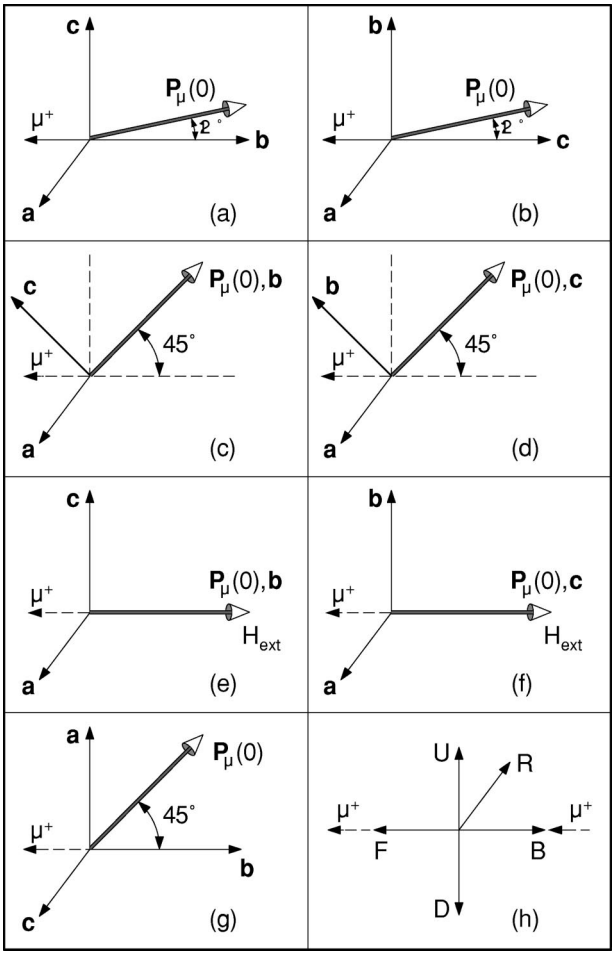

FIG. 1. Schematic view of the relative sample and $\boldsymbol{P}_\mu(0)$ orientations used in the ZF measurements. Panels (e), (f) refer also to the orientations in the LF case. The indicated values of α were determined by weak TF measurements with $\boldsymbol{H}_{ext}\|\boldsymbol{z}$ axis. Panel h sketches the arrangement of the five positron detectors.

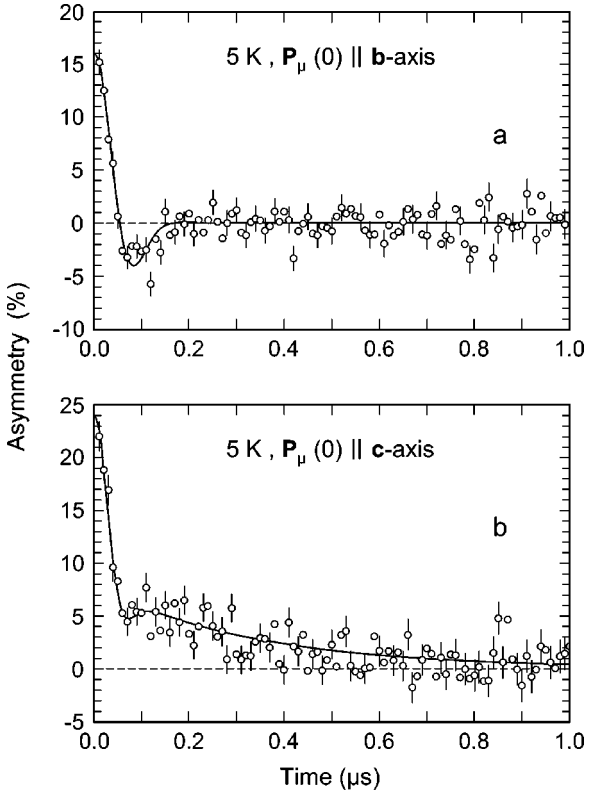

FIG. 2. The time evolution of the μ^+ polarization $P(t)$ in the forward/backward direction at 5 K for (a) $\boldsymbol{P}_\mu \| \boldsymbol{b}$ axis and (b) $\boldsymbol{P}_\mu(0) \| \boldsymbol{c}$ axis. The solid lines are fits of Eq. (2) to the data.

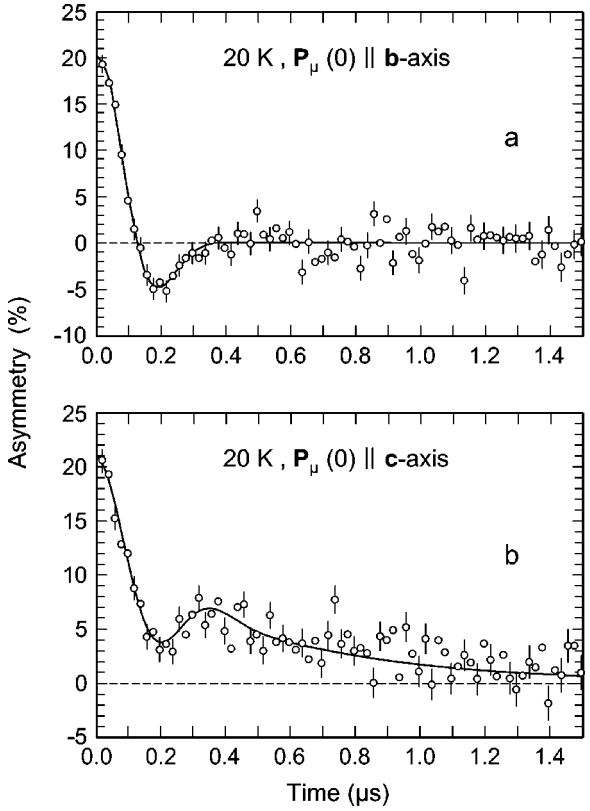

FIG. 3. Same as Fig. 2 but measured at 20 K.

1(h). Both instruments, by means of cleverly arranged veto detectors, allow us to measure essentially free of a background signal arising from μ^+ failing to stop in the sample. The LTF is equipped with forward/backward, left and right positron detectors. We only used the first two detectors. In the GPD, we made use of forward/backward, up/ down detectors and the cryostat was in this case a closed cycle refrigerator, inserted horizontally into the spectrometer (minimum temperature = 10 K).

Several single crystals of $PrCu_2$ were at our disposal, all grown at Osaka University as described in Ref. 8. The purity of the starting material amounted to 99.99% for Pr, with impurity contents of Ce (2 ppm), Ni (4 ppm), and Fe (20 ppm), to 99.999% for Cu, with no traceable amounts of magnetic impurities. Most measurements were performed with a cylindrical sample with 6 mm diameter and 25 mm length. The cylinder axis coincided with the crystallographic *a* axis. This sample was used in GPS, Dolly, and GPD. In the GPS and Dolly, the sample could be rotated around the *a* axis oriented perpendicular to the beam, or to the applied field H_{ext} in the horizontal plane. Hence the initial μ^+ polarization at the time of implantation $\boldsymbol{P}_\mu(0)$ or $\boldsymbol{H}_{ext}$ could be turned in the (b,c) plane. This sample was also used in the GPD where $\boldsymbol{H}_{ext}$ was coinciding with the *a* axis. The sample was too large to fit into the dilution refrigerator of the LTF and here we used an assembly of three small flat single crystalline plates of rectangular shape with the short side pointing along the *c* axis, the long side along the *a* axis, and the *b* axis perpendicular to the plate plane and parallel to the incoming μ^+. This sample was also used in the GPS with the *a* axis along the vertical direction such that $\boldsymbol{P}_\mu(0)$ fell into the (a,b) plane. For more information on the used spectrometers, refer to (Ref. 29).

As usual in a μSR experiment the evolution of the μ^+ polarization $\boldsymbol{P}(t)$ is monitored via the time-dependent decay asymmetry of the implanted μ^+ by observing the positrons from the μ^+ decay in a certain direction $\boldsymbol{r}$ as a function of elapsed μ^+ lifetime. The positron rate can then be written as[13]

$$\frac{dN_{e^+}(t)}{dt} = \frac{1}{4\pi\tau_\mu} N_0 e^{-t/\tau_\mu}(1 - A\boldsymbol{P}(t)\cdot\boldsymbol{r}) d\Omega_r, \qquad (1)$$

where A is the effective decay asymmetry (0.2–0.3), τ_μ the mean muon lifetime (2.2 μs), $|\boldsymbol{r}| = 1$, and $d\Omega_r$ a solid angle element in the direction of $\boldsymbol{r}$. In the following, we will often call $AP(t) \equiv A\boldsymbol{P}(t)\cdot\boldsymbol{r}$ asymmetry or signal amplitude.

III. ZF AND LF MEASUREMENTS

A. Overview

In ZF the temperature dependence of $P(t)$ was measured for the sample orientations displayed in Fig. 1. For the measurements in the LTF (down to 20 mK) the orientation corresponded to Fig. 1(a). Angular scans in ZF were performed by rotating the sample around the *a* axis, [i.e., $\boldsymbol{P}_\mu(0)$ rotated in the (b,c) plane] at 2 K, 5 K, 20 K, 23 K, and 50 K. LF measurements were performed at 2 K, 5 K, 7 K, 8 K, 10 K, 15 K, 20 K, 30 K, 40 K, 50 K, 60 K, 70 K, and 80 K for

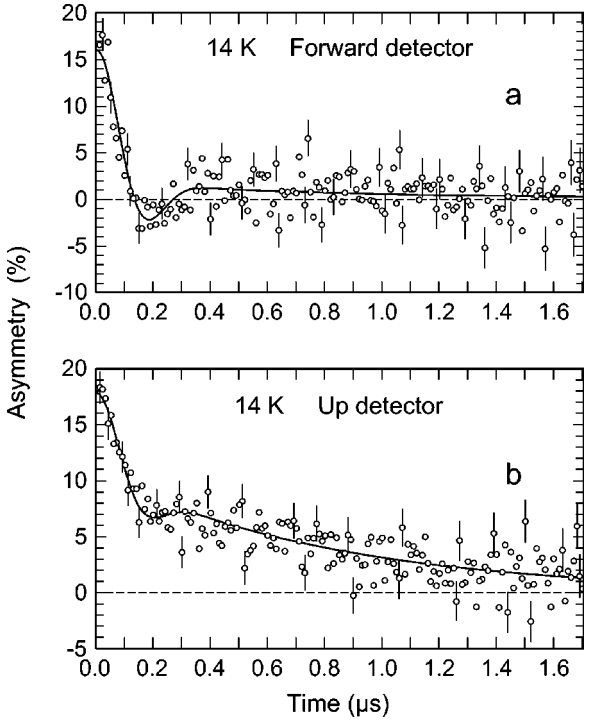

FIG. 4. Time evolution of $P_\mu(t)$ in (a) the forward and (b) the up detector at 14 K for the arrangement shown in Fig. 1(g).

$\boldsymbol{H}_{ext}\|\boldsymbol{P}_\mu(0)\|\boldsymbol{c}$ axis and at 2 K, 5 K, 7 K, 8 K, 10 K, 15 K, 20 K, 30 K, 50 K, and 80 K for $\boldsymbol{H}_{ext}\|\boldsymbol{P}_\mu(0)\|\boldsymbol{b}$ axis, respectively. The field scans, depending on temperature, extended up to 4 kOe. We performed also temperature scans in LF (ranging up to 4 kOe) for $\boldsymbol{b}$ axis $\|\boldsymbol{H}_{ext}$ and $\boldsymbol{c}$ axis $\|\boldsymbol{H}_{ext}$.

B. ZF results

Figures 2–4 show some typical $AP(t)$ obtained at 5 K, 14 K, and 20 K. Figure 2 and 3 demonstrate that the signals depend very much on the orientation, and Fig. 4 shows that it also matters in which direction the signal is observed. Generally $P(t)$ is well fitted by the expression

$$P(t)=A_\omega\exp\left(-\frac{1}{2}\sigma^2t^2\right)\cos\omega t+A_\lambda\exp(-\lambda t), \qquad (2)$$

with $A_\omega+A_\lambda=1$, where A_λ approaches zero when $\boldsymbol{P}_\mu(0)\|\boldsymbol{b}$ axis. Clearly, a precession signal is observed which implies that a nonzero spontaneous magnetic field is present in the sample. It is also recognized immediately that the internal fields must possess a wide distribution in view of the fast damping of the precession component, which appears to be well represented by a Gaussian decay function.

The orientation dependence of A_ω and A_λ is measured in detail by angular scans. Figures 5(a) and 5(b) show the results obtained at 2 K and 23 K. In the first case, $\boldsymbol{P}_\mu(0)$ was parallel to the beam axis, i.e., the projection of $\boldsymbol{P}_\mu(0)$ in the up and down directions should be zero. Nevertheless, a signal is seen also in the up and down detectors (Fig. 6). In the second case, $\boldsymbol{P}_\mu(0)$ was rotated away from the beam axis by 12° so that at time zero, a nonzero net component in the up

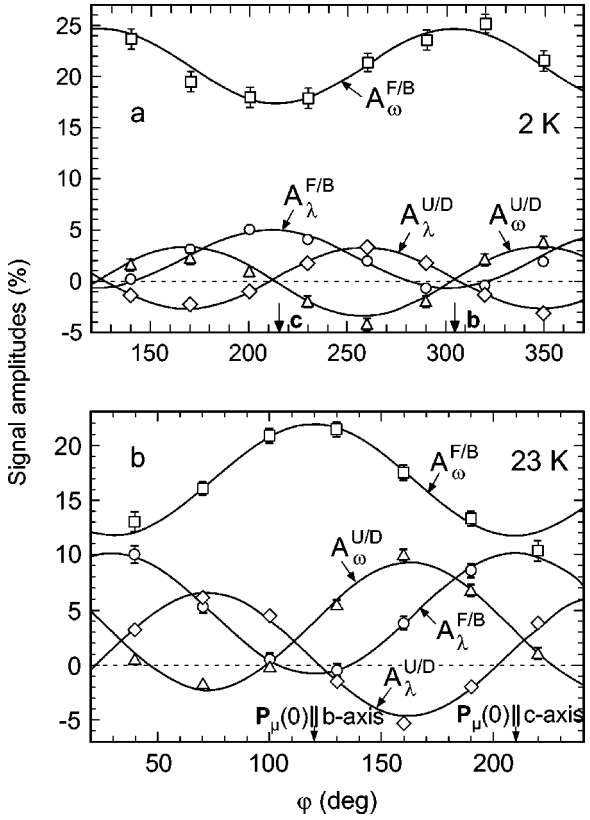

FIG. 5. Orientation dependence of the amplitudes $A_\omega^{F/B}$,$A_\lambda^{F/B}$ in forward/backward direction and of $A_\omega^{U/D}$,$A_\lambda^{U/D}$ in up/down direction, respectively, at (a) 2 K and (b) 23 K. $\boldsymbol{P}_\mu(0)$ rotates in the (b,c) plane. The solid lines are fits of Eqs. (12) and (13) to the data yielding generally $\phi=0°\pm3°$ and $\theta=33°\pm2.3°$ at 2 K and $\theta=43.7°\pm2.2°$ at 23 K.

and down directions existed. A comparison of the two figures shows that temperature has a pronounced effect on the anisotropy of A_λ and A_ω. At 2 K the average A_ω is larger and the average A_λ smaller, and the modulation of both is significantly smaller than at 20 K. Note that at a given T the modulation is the same for A_λ and A_ω independent of whether the signal is observed in the forward/backward or up/down directions. It should also be mentioned that no signal was seen in the right direction. We will see in the follow-

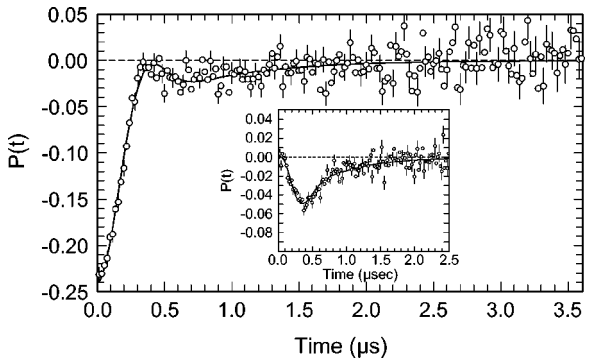

FIG. 6. Time evolution of μ^+ polarization [arrangement Fig. 1(e)] in forward/backward and (inset) up/down direction at 30 K.

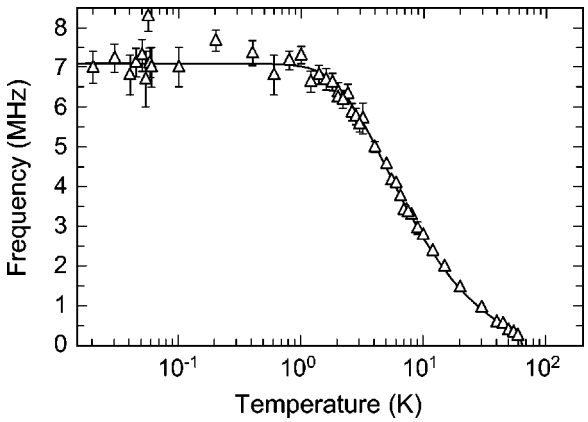

FIG. 7. Temperature dependence of the spontaneous frequency $\omega/2\pi$. The solid line is a fit of Eq. (3) to the data.

ing section that the observed angular dependencies will allow us to determine the direction of the spontaneous field $\boldsymbol{B}$ with respect to the crystal axes.

The second nonoscillating but exponentially relaxing component in Eq. (2) must reflect the projection of $\boldsymbol{P}_\mu(0)$ onto the internal field $\boldsymbol{B}$ which will only become time dependent when fluctuating field components perpendicular to $\boldsymbol{B}$ are present and are able to induce spin-lattice relaxation.

The temperature dependence of the fitted precession frequency is displayed in Fig. 7. The temperature dependence is perfectly fitted by the expression

$$\nu(T)=\nu_0\left[1-\exp\left(\frac{-E}{kT}\right)\right]\left(1-\frac{T}{T_{cr}}\right)^{\beta}, \tag{3}$$

with $E=5.15\pm0.05$ K, $\beta=0.38\pm0.04$, and $T_{cr}=64\pm2$ K. The discussion of this result is deferred to Sec. V C. The temperature dependence of σ is displayed in Fig. 8. We note that σ depends on the sample orientation. Between 2 K and 65 K, the data are well fitted by the equation

$$\sigma=\sigma(0)\frac{1}{T^{\beta}}+\sigma_0, \tag{4}$$

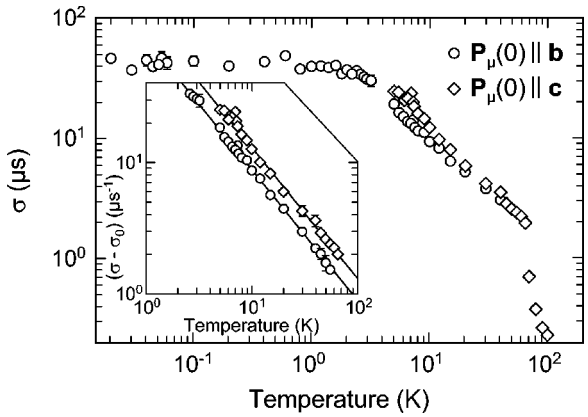

FIG. 8. Temperature dependence of the Gaussian relaxation rate σ. The inset shows a log-log plot of $(\sigma-\sigma_0)$ versus temperature for $2<T<70$ K. The straight lines have a slope of -1. Note the slight anisotropy of σ (see text).

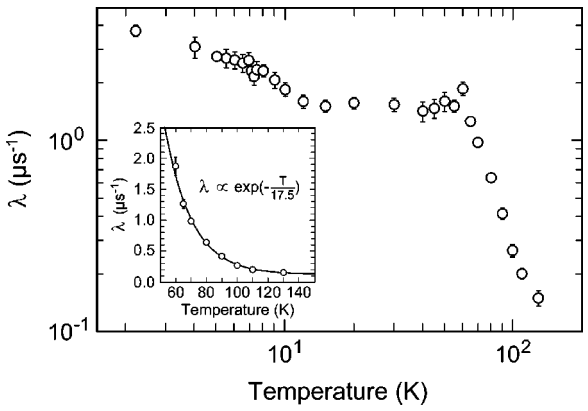

FIG. 9. Temperature dependence of the spin-lattice relaxation rate λ in ZF. The inset shows λ above 60 K, the solid line represents an exponential fit.

with $\beta=1.01\pm0.03$ and $\sigma(0)=89\pm5$ μs^{-1} for both orientations, whereas the constant σ_0 is orientation dependent, i.e., zero for $\boldsymbol{P}_\mu(0)\|\boldsymbol{c}$ axis and 0.91 ± 0.16 μs^{-1} for $\boldsymbol{P}_\mu(0)\|\boldsymbol{b}$ axis. The inset in Fig. 8 shows a log-log plot of $(\sigma-\sigma_0)$ versus temperature and demonstrates nicely the T^{-1} dependence. This will be discussed further in Sec. V C. To a certain extent, $\sigma(T)$ looks similar to $\nu(T)$ but Eq. (3) does not allow a proper fit of $\sigma(T)$. One important difference is that $\nu(T)$ vanishes at 65 K, but not $\sigma(T)$. In fact, between 80 K and 130 K Eq. (2) has to be replaced by the expression

$$P(t)=A_\lambda\exp\left[-\left(\frac{1}{2}\sigma^2t^2+\lambda t\right)\right], \tag{5}$$

and σ seems to be finally arising from the random field spread due to the Cu and Pr nuclear moments. We will not discuss this further.

The temperature dependence of the spin-lattice relaxation rate λ for $\boldsymbol{P}_\mu(0)\|\boldsymbol{c}$ axis is shown in Fig. 9. Since for $\boldsymbol{P}_\mu(0)\|\boldsymbol{b}$ axis in ZF the second term in Eq. (2) is absent, we cannot determine λ for this orientation. However, the angular scans show that λ in ZF must be essentially isotropic. Anisotropy will appear when a longitudinal field is applied (see below). Interestingly the ZF λ, displayed in Fig. 9, shows relatively little temperature dependence below 60 K but a cusplike anomaly at ~60 K and sharp exponential decrease above that temperature (see inset in Fig. 9). For details, refer to Secs. III E and V B.

C. Discussion of the anisotropy of $P(t)$

The dependence of $\boldsymbol{P}(t)$ on the orientation of the initial μ^+ polarization $\boldsymbol{P}_\mu(0)$ with respect to the crystal frame is naturally to be expected when the angle between the internal field $\boldsymbol{B}$ and $\boldsymbol{P}_\mu(0)$ or the aperture of the precession cone and its axis, respectively, change. The time evolution of the μ^+ polarization can most generally be expressed as[14]

$$\boldsymbol{P}(t)=[\boldsymbol{P}_\mu(0)\cdot\boldsymbol{b}]\boldsymbol{b}+\{\boldsymbol{P}_\mu(0)-[\boldsymbol{P}_\mu(0)\cdot\boldsymbol{b}]\boldsymbol{b}\}\cos\omega t + [\boldsymbol{P}_\mu(0)\times\boldsymbol{b}]\sin\omega t, \tag{6}$$

where $\boldsymbol{b}=\boldsymbol{B}/B$ and $\omega=\gamma_\mu B$ [$\gamma_\mu=(2\pi)13.55$ kHz/G].

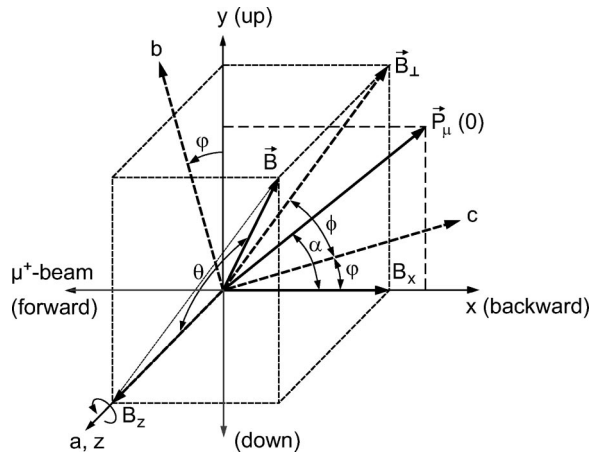

FIG. 10. This figure shows the used (x,y,z)-coordinate system and the crystal frame, where y is oriented in the vertical direction and x along the horizontal μ^+ beam axis. The crystalline a axis of the $PrCu_2$ sample coincides with the z axis around which the sample can be rotated, changing the angle φ. The crystalline (b,c) plane coincides with the (x,y) plane. The initial μ^+ polarization $\boldsymbol{P}_\mu(0)$ is located in the (x,y) plane and encloses an angle of α with the x axis. Also indicated is some internal field $\boldsymbol{B}$ whose direction is defined via the angles θ and ϕ, e.g., $B_c = B \sin\theta\cos\phi$, etc.

The third term will be absent in an antiferromagnet since to each $\boldsymbol{B}$ there will be a $-\boldsymbol{B}$ and we will have as many μ^+ precessing clockwise and counter clockwise.

Along the direction of observation $\boldsymbol{r}$, the amplitudes of the nonoscillating and the oscillating terms will be given by

$$A_\lambda = [\boldsymbol{P}_\mu(0)\cdot\boldsymbol{b}](\boldsymbol{b}\cdot\boldsymbol{r}) \tag{7}$$

and

$$A_\omega = \boldsymbol{P}_\mu(0)\cdot\boldsymbol{r} - A_\lambda\,. \tag{8}$$

We introduce a laboratory frame x,y,z as shown in Fig. 10, and a crystal frame (a,b,c) such that the a axis is parallel to the z axis around which the crystal can be rotated. Using polar coordinates, $\boldsymbol{B}$ can be expressed in the crystal frame as

$$\boldsymbol{B} = B[\sin\theta(\cos\phi\,\hat{\boldsymbol{b}} + \sin\phi\,\hat{\boldsymbol{c}}) + \cos\theta\,\hat{\boldsymbol{c}}], \tag{9}$$

where $\hat{\boldsymbol{a}},\hat{\boldsymbol{b}}$, and $\hat{\boldsymbol{c}}$ are unit vectors along the crystal axes a,b,c. In the laboratory frame,

$$\boldsymbol{B} = B\{\sin\theta[\cos(\phi+\varphi)\hat{\boldsymbol{x}} + \sin(\phi+\varphi)\hat{\boldsymbol{y}}] + \cos\theta\,\hat{\boldsymbol{z}}\}, \tag{10}$$

where φ is the angle between the c axis and the x axis, (=beam axis), which will change when the crystal is rotated around the a axis or the z axis, respectively. $\hat{\boldsymbol{x}},\hat{\boldsymbol{y}},\hat{\boldsymbol{z}}$ are unit vectors along the x,y, and z axis. The initial polarization $\boldsymbol{P}_\mu(0)$, restricted in the experiment to the vertical (x,y) plane, will be given by

$$\boldsymbol{P}(0) = P_\mu(0)(\cos\alpha\,\hat{\boldsymbol{x}} + \sin\alpha\,\hat{\boldsymbol{y}}) \tag{11}$$

and $\boldsymbol{r}$ in forward/backward, up/down, and right direction by

$$\boldsymbol{r}_{F/B} = [\mp 1,0,0], \quad \boldsymbol{r}_{U/D} = [0,\pm 1,0], \quad \text{and} \quad \boldsymbol{r}_R = [0,0,-1].$$

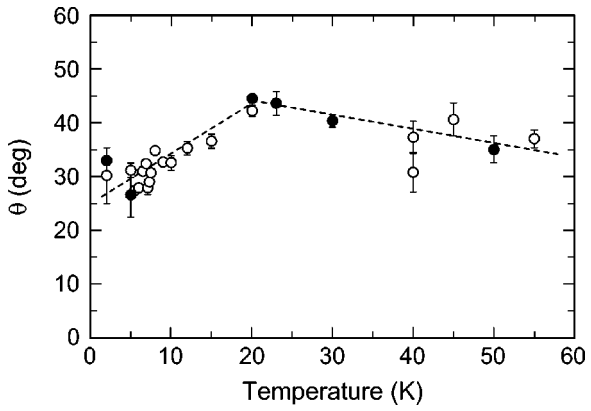

FIG. 11. Temperature dependence of angle θ, i.e., the angle between $\boldsymbol{B}$ and the a axis.

For those directions of observation the amplitudes [Eqs. (7) and (8)] assume the expressions

$$A_\lambda^{F/B}(\varphi) = \mp A\frac{1}{2}\sin^2\theta\{\cos\alpha + \cos[2(\phi+\varphi)-\alpha]\}, \tag{12a}$$

$$A_\lambda^{U/D}(\varphi) = \pm A\frac{1}{2}\sin^2\theta\{\sin\alpha + \sin[2(\phi+\varphi)-\alpha]\}, \tag{12b}$$

$$A_\lambda^{R}(\varphi) = -A\frac{1}{2}\sin(2\theta)\cos(\phi+\varphi-\alpha) \tag{12c}$$

and

$$A_\omega^{F/B}(\varphi) = \mp A\cos\alpha - A_\lambda^{F/B}(\varphi), \tag{13a}$$

$$A_\omega^{U/D}(\varphi) = \pm A\sin\alpha - A_\lambda^{U/D}(\varphi), \tag{13b}$$

$$A_\omega^{R}(\varphi) = -A_\lambda^{R}(\varphi). \tag{13c}$$

The value of α, i.e., the direction of $\boldsymbol{P}_\mu(0)$, and of the decay asymmetry A can be determined by calibration measurements in weak fields applied parallel to the z axis, i.e., perpendicular to $\boldsymbol{P}_\mu(0)$. Hence fitting Eqs. (12) and (13), to experimental data the only free parameters are the angles θ and ϕ. In particular, the relative ratio of the φ-dependent and φ-independent terms in Eqs. (12) and (13) are fixed by the angle α. For the various arrangements, the calibrated α are also indicated in Fig. 1. All angular scans, independent of the used temperature, are excellently fitted by Eqs. (12) and (13), as demonstrated by the solid lines in Fig. 5. The corresponding fit parameters are reported in the figure caption. Generally we find $\phi = 0$, while θ becomes temperature dependent and varies between $\sim 30°$ and $\sim 45°$ (see Fig. 11 and discussion below). For other temperatures, $\sin^2\theta$ or θ, respectively, was extracted from the amplitudes of the oscillating component, $A_\omega/A \propto \sin^2\theta$. We mention that similar data obtained in $CeRhIn_5$ could not be fitted by Eqs. (12) and (13). In this case a conical arrangement of the internal fields had to be admitted and correspondingly modified Eqs. (12) and (13) then fitted the data perfectly.[14] The choice of α has a decisive

effect on the observable signal. For example, if $\alpha=45°$ and $\varphi=45°$ [Fig. 1(d)], we find $|A_\lambda^{F/B}|=A\sin^2\theta=|A_\lambda^{U/D}|$ and $|A_\omega^{F/B}|=A(\cos 45°-\sin^2\theta)=|A_\omega^{F/B}|$, i.e., the oscillating and nonoscillating components are the same in forward/backward and up/down directions.

This is indeed observed in the GPS. If on the other hand $\alpha=0$, as in the Dolly instrument, and $\varphi=0°$ [Fig. 1(f)], we have $|A_\lambda^{F/B}|=A\sin^2\theta$, $A_\lambda^{U/D}=0$ and $|A_\omega^{F/B}|=A(1-\sin^2\theta)$, $A_\omega^{U/D}=0$, i.e., no signal is seen in the up/down directions. If $\alpha=0$ and $\varphi=45°$, we find $|A_\lambda^{F/B}|=\frac{1}{2}A\sin^2\theta$, $|A_\lambda^{U/D}|=\frac{1}{2}A\sin^2\theta$ and $|A_\omega^{F/B}|=-A(1-\frac{1}{2}\sin^2\theta)$, $|A_\omega^{U/D}|=\frac{1}{2}A\sin^2\theta$. This situation, which leads to $A_\omega^{U/D}=-A_\lambda^{U/D}$, is realized indeed for the signals in Fig. 6. For another configuration where the *c* axis coincides now with the *z* axis and the *a* axis points along the vertical *y* axis [Fig. 1(g)] (this changes ϕ to 90° and $\varphi=0°$ is now the angle between the *x* axis and the *b* axis), we find for $\alpha=45°$, $A_\lambda^{F/B}=0$, $|A_\lambda^{U/D}|=A\sin 45°(\sin^2\theta)$ and $|A_\omega^{F/B}|=A\cos 45°$, $|A_\omega^{U/D}|=A\sin 45°(1-\sin^2\theta)$, i.e., in the forward/backward direction only the oscillating term is expected to be seen, while in the up/down direction both terms should be superimposed. The data in Fig. 4 show precisely this behavior. Equations (12c) and (13c) predict that a sizable signal with a periodicity of 360° should be well visible in the right direction as long as $\theta\neq 0°$ or 90°. No such signal is, in fact, detectable. This caused some serious concern, but we will later see that it is a natural consequence of a distribution of θ values, owing to the modulated structure of the magnetic order and the $\sin 2\theta$ factor. Note that for the other orientations the $\sin\theta$ factor appears quadratically. Hence the fitted θ values have to be viewed as averages over their absolute values.

We are now in a position to provide a first description of the internal field distribution. The angle $\phi=0°$ implies that the projection of $\boldsymbol{B}$ onto the (b,c) plane is parallel to the *c* axis and hence $\boldsymbol{B}$ must be confined to the (a,c) plane. The average deviation from the *a* axis (the *z* axis in our geometry) is temperature dependent and changes as shown in Fig. 11. Since θ is extracted from $\sin^2\theta$, θ may be positive as well as negative. The absence of any detectable signal in the right direction indicates strongly that θ may indeed vary between positive and negative values so that the average of $\sin 2\theta$ can become quite small or even zero. Further evidence for a distribution of θ values is provided by measurements in a longitudinal field.

D. Measurements in longitudinal fields

Information on the direction of internal fields can also be obtained by applying an external field $\boldsymbol{H}_{ext}$ and monitoring the μ^+ Larmor precession around the new total field $\boldsymbol{B}+\boldsymbol{H}_{ext}$.[15] This works only in systems which do not possess a multidomain structure such that $\boldsymbol{B}$ appears randomly oriented. It also requires use of single crystals. Both conditions are fulfilled for the present system. The field $\boldsymbol{H}_{ext}$ was applied either parallel to the *c* axis ($\varphi=0$) or parallel to the *b* axis ($\varphi=90°$) with $\boldsymbol{P}_\mu(0)$ parallel to $\boldsymbol{H}_{ext}$ (in Dolly). Replacing in Eqs. (7) and (8) $\boldsymbol{B}$ by $\boldsymbol{B}+\boldsymbol{H}_{ext}$, we calculate for these orientation

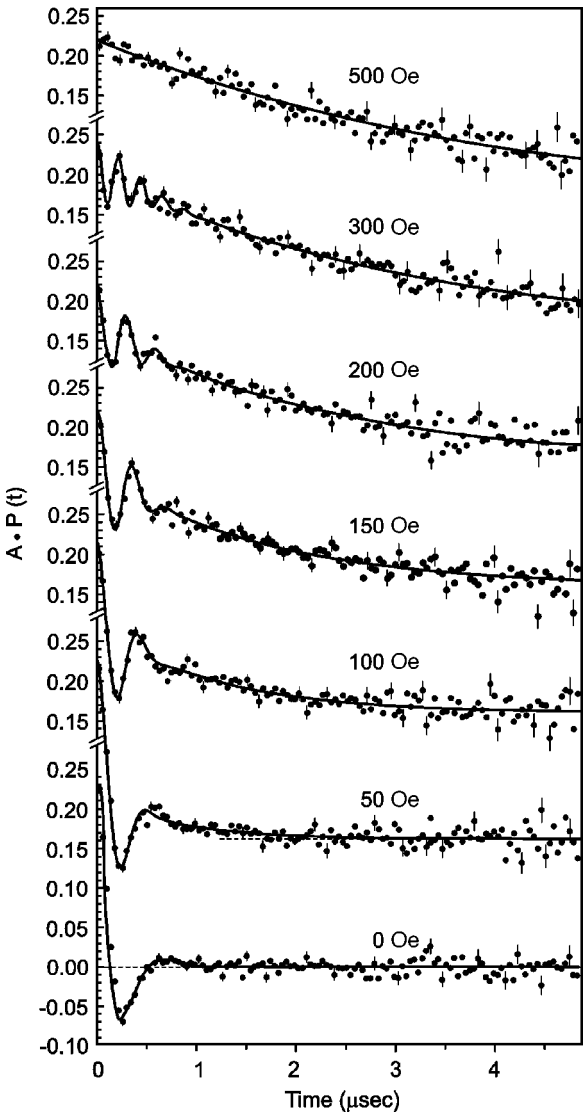

FIG. 12. μSR signals in backward direction at 20 K for various longitudinal fields. The solid lines represent fits of Eq. (2) to the data.

$$A_\lambda^{F/B}(\varphi=0^\circ)=A\frac{(B\sin\theta\pm H_{ext})^2}{B^2+H_{ext}^2\pm H_{ext}B\sin\theta}, \tag{14a}$$

$$A_\omega^{F/B}(\varphi=0^\circ)=A-A_\lambda^{F/B}(\varphi=0°), \tag{14b}$$

$$A_\lambda^{F/B}(\varphi=90°)=A\frac{H_{ext}^2}{B^2+H_{ext}^2}, \tag{15a}$$

$$A_\omega^{F/B}(\varphi=90°)=A-A_\lambda^{F/B}(\varphi=90°), \tag{15b}$$

and the total field at the μ^+ will be

$$B_{tot}(\varphi=0°)\sqrt{B^2+H_{ext}^2\pm 2H_{ext}B\sin\theta}, \tag{16}$$

$$B_{tot}(\varphi=90°)=\sqrt{B^2+H_{ext}^2}. \tag{17}$$

The $\pm$ sign appears in Eqs. (14a) and (16) because of the overall antiferromagnetic moment arrangement leading to

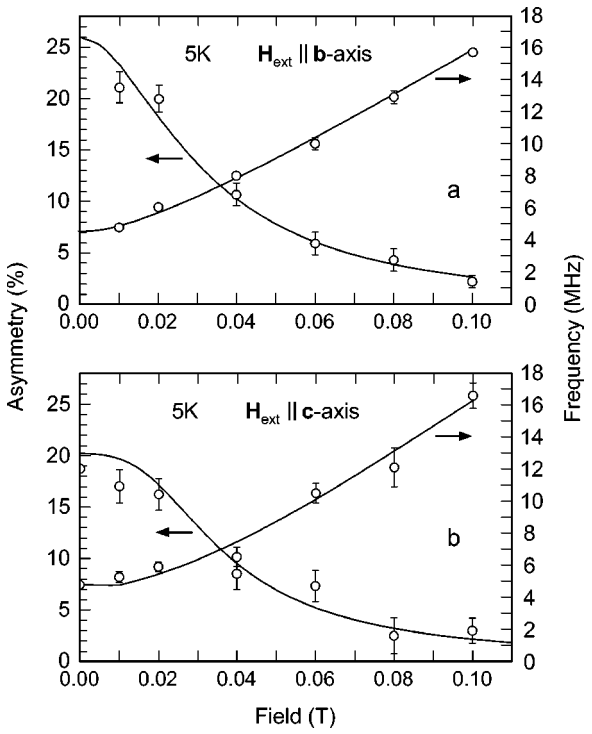

FIG. 13. Field dependence of the amplitude A_ω and the precession frequency $\omega/2\pi$ at 5 K for (a) $\boldsymbol{H}_{ext}\|\boldsymbol{b}$ axis and (b) $\boldsymbol{H}_{ext}\|\boldsymbol{c}$ axis. The solid lines are calculated as discussed in Sec. V A.

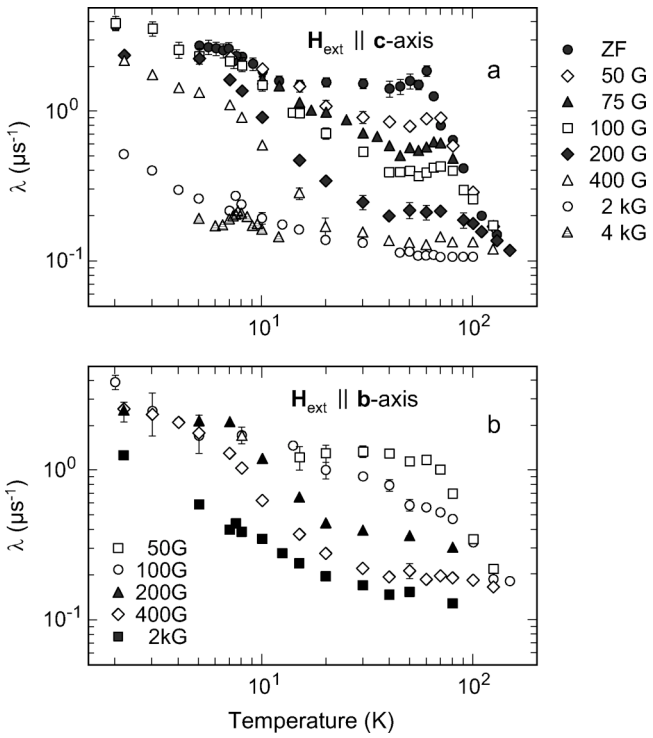

FIG. 14. Temperature dependence of λ at various longitudinal fields for (a) $\boldsymbol{H}_{ext}\|\boldsymbol{c}$ axis and (b) $\boldsymbol{H}_{ext}\|\boldsymbol{b}$ axis.

fields $+\boldsymbol{B}$ and $-\boldsymbol{B}$ in the (a,c) plane. For $\boldsymbol{H}_{ext}$ in the (a,c) plane, this implies resulting fields $\boldsymbol{H}_{ext}\pm\boldsymbol{B}$. For $\boldsymbol{H}_{ext}$ perpendicular to the (a,c) plane, the sign of $\boldsymbol{B}$ does not matter and B_{tot} is simply given by Eq. (17). Hence in the former case we expect a splitting of the oscillating component.

Figure 12 shows a sequence of signals $AP(t)$ in backward direction for $\boldsymbol{b}$ axis $\|\boldsymbol{H}_{ext}$ at 20 K with H_{ext} ranging from zero to 500 Oe. All signals are fitted well (solid lines) by Eq. (2). As examples the field dependence of A_ω and of the precession frequency $\omega/2\pi$ are displayed in Figs. 13(a) and 13(b) for $T=5$ K, respectively. $A_\omega(H_{ext})$ and $\omega(H_{ext})/2\pi$ for $\boldsymbol{H}_{ext}\|\boldsymbol{b}$ axis are reasonably well fitted by Eqs. (15b) and (17). The solid lines shown in Fig. 13(a), however, stem from calculations discussed in Sec. V A. Note that $A_\lambda^{F/B}=0$ for $H_{ext}=0$ and increases with increasing H_{ext} by the same proportion that $A_\omega^{F/B}$ decreases in accordance with Eqs. (15a) and (15b).

Very similar results are obtained for $\boldsymbol{H}_{ext}\|\boldsymbol{c}$ axis except that $A_\lambda^{F/B}$ is different from zero already at $H_{ext}=0$. Equation (2) allows still excellent fits and there is no indication for a splitting as predicted above. The field dependence of A_ω and $\omega/2\pi$ is displayed in Fig. 13(b). In particular, $A_\omega(H_{ext})$ is not following Eq. (14b) averaged over the + and − sign versions. Note that $A_\omega=0$ for $B\cos\theta-H_{ext}=0$. This outcome is another indication that $\boldsymbol{B}$ shows a more complex distribution. As we will see in Sec. V A, $A_\omega^{F/B}(H_{ext})$ and $\omega(H_{ext})/2\pi$ can be well reproduced on the basis of the considered magnetic structure [solid lines in Fig. 13(b)].

E. Temperature and field dependence of λ

The LF scans at various temperatures allow also to determine the corresponding dependencies of the spin-lattice relaxation rate λ. Figures 14(a) and 15(b) provide an overall view of $\lambda(T,H_{ext})$ for $\boldsymbol{H}_{ext}\|\boldsymbol{c}$ axis and $\boldsymbol{H}_{ext}\|\boldsymbol{b}$ axis, respectively. Figure 15(a) compares the anisotropy of λ for $H_{ext}=100$ Oe and 2 kOe. Generally λ decreases with increasing H_{ext} but the anisotropy becomes more pronounced. For smaller H_{ext} the anisotropy is limited to the range 15–60 K, but for $H_{ext}>400$ Oe, λ is anisotropic from at least 2 K up to at least 130 K [see Fig. 15(b)]. While the temperature dependence of λ for $H_{ext}\leqslant 400$ Oe looks complex, a $1/T$ dependence is seen for $H_{ext}=2$ kOe. The solid lines in Fig. 15(b) are fits of the expression

$$\lambda=\frac{\lambda_0}{T}+\text{const} \tag{18}$$

to the data. For both orientations const$=0.095(1)$ μs^{-1} and $\lambda_0(\boldsymbol{H}_{ext}\|\boldsymbol{b})/\lambda_0(\boldsymbol{H}_{ext}\|\boldsymbol{c})=4.0(4)$. We notice a weak anomalous feature at 7.5 K, i.e., at T_{JT}. This becomes much more pronounced in a field of $H_{ext}=4$ kOe. [see inset in Fig. 15(b)]. This anomaly is absent for $H_{ext}\leqslant 400$ Oe.

The field dependence of λ at all temperatures and for both orientations follows the expression

$$\lambda(H_{ext})=\lambda_0\frac{1}{1+(\tau\omega)^2}+\lambda_{con}, \tag{19}$$

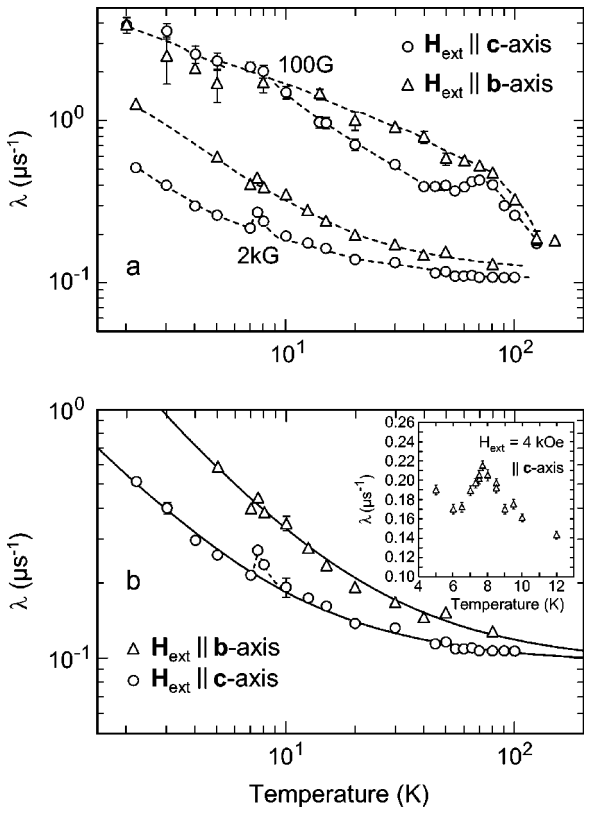

FIG. 15. (a) Comparison of $\lambda(T)$ in LF at 100 Oe and 2 kOe for the two orientation $\boldsymbol{H}_{ext}\|\boldsymbol{c}$ axis and $\boldsymbol{H}_{ext}\|\boldsymbol{b}$ axis. (b) Temperature dependence of λ in LF at 2 kOe for $\boldsymbol{H}_{ext}\|\boldsymbol{b}$ axis and $\boldsymbol{H}_{ext}\|\boldsymbol{c}$ axis. The solid lines represent fits of Eq. (18) to the data. Note the anomaly near $T_{JT}=7.5$ K which is much more pronounced at 4 kOe (inset).

with $\omega=\gamma_\mu H_{ext}$. For $\boldsymbol{H}_{ext}\|\boldsymbol{c}$ axis the data and the fits are displayed in Fig. 16. These results will be discussed further in Sec. V B.

IV. TRANSVERSE-FIELD MEASUREMENTS

A. Experimental results

These measurements were primarily conducted with the aim to determine the μ^+ site in $PrCu_2$ from the μ^+ Knight

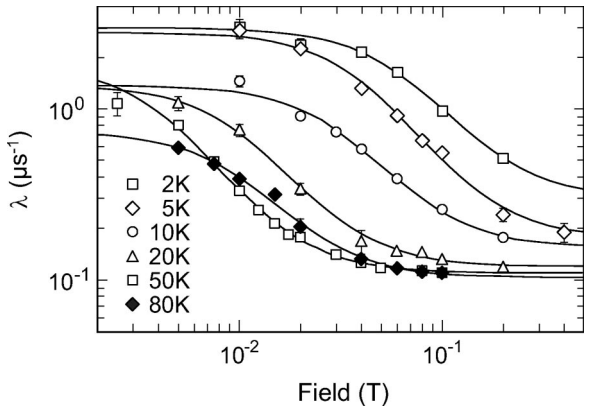

FIG. 16. Longitudinal-field dependence of λ at various temperatures for $\boldsymbol{H}_{ext}\|\boldsymbol{c}$ axis. The solid lines are fits of Eq. (19) to the data.

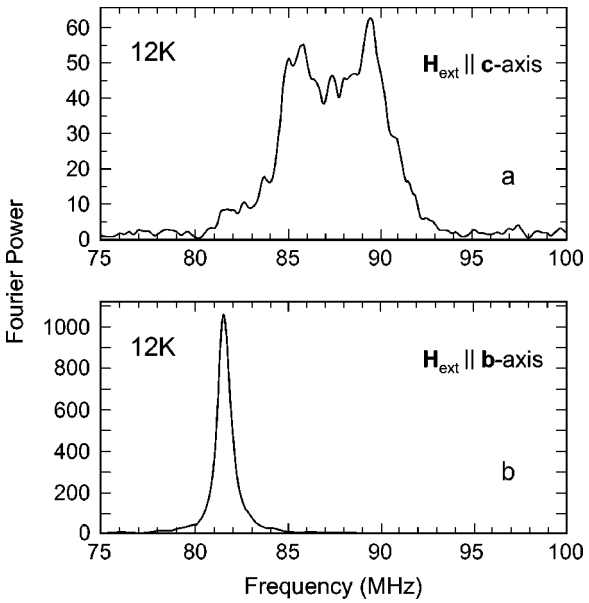

FIG. 17. Fourier transform of the TF signal at 12 K ($H_{ext}=6$ kOe) for (a) $\boldsymbol{H}_{ext}\|\boldsymbol{c}$ axis and (b) $\boldsymbol{H}_{ext}\|\boldsymbol{b}$ axis.

shift in the usual way.[16] The muon precession frequency was measured for $\boldsymbol{H}_{ext}\|\boldsymbol{b}$ axis, $\boldsymbol{H}_{ext}\|\boldsymbol{c}$ axis ($H_{ext}=6$ kOe) and for $\boldsymbol{H}_{ext}\|\boldsymbol{a}$ axis ($H_{ext}=4$ kOe) in the temperature range 2(10) $-300(320)$ K. Figure 17 displays Fourier transforms of the precession signal taken for $\boldsymbol{H}_{ext}\|\boldsymbol{c}$ axis and $\boldsymbol{H}_{ext}\|\boldsymbol{b}$ axis at 12 K. In the latter case, a single relatively narrow line is observed, while in the former case two rather broad and closely spaced lines seem to be present. The precession signal is indeed best fitted for $T<60$ K by a two-component function

$$P_c(t)=A_1 e^{-(1/2)\sigma_1^2 t^2}\cos\omega_1 t+A_2 e^{-(1/2)\sigma_2^2 t^2}\cos\omega_2 t \tag{20}$$

and it is found that $A_2=A_1$ and $\sigma_2=\sigma_1$. Above 60 K the two components merge into a single line. The temperature dependence of $\omega_1/2\pi$ and $\omega_2/2\pi$ is displayed in Fig. 18(a). In accord with the Fourier transform for $\boldsymbol{H}_{ext}\|\boldsymbol{b}$ axis, the precession signal is perfectly fitted by a one-component function

$$P_b(t)=A e^{-(1/2)\sigma_3^2 t^2}\cos\omega_3 t. \tag{21}$$

The temperature dependence of $\omega_3/2\pi$ is displayed in Fig. 18(b). The difference $\omega_1-\omega_2$ scales well with the frequency ω_{ZF} of the spontaneous ZF signal below 60 K and in fact, seems to be equal to ω_{ZF} [see inset in Fig. 18(a)]. Since for the orientation $\boldsymbol{H}_{ext}\|\boldsymbol{c}$ axis $\boldsymbol{H}_{ext}$ and the internal fields $\boldsymbol{B}$ are coplanar, we expect, as in the LF case, that the total field will assume two values according to Eq. (16). We will later see in Sec. V A that in contrast to the LF signals, a split TF signal in a strong H_{ext} ($H_{ext}>B$) is indeed predicted. A split signal is also expected for the orientation $\boldsymbol{H}_{ext}\|\boldsymbol{a}$ axis, but since the quality of the spectra in the GPD were much poorer we did not attempt to perform two-component fits. For the other orientation ($\boldsymbol{H}_{ext}\|\boldsymbol{b}$) $\boldsymbol{H}_{ext}$ is perpendicular to $\boldsymbol{B}$ and no splitting will occur, hence a single line is observed. As can be seen $\omega_3/2\pi$ is shifted to values below the frequency

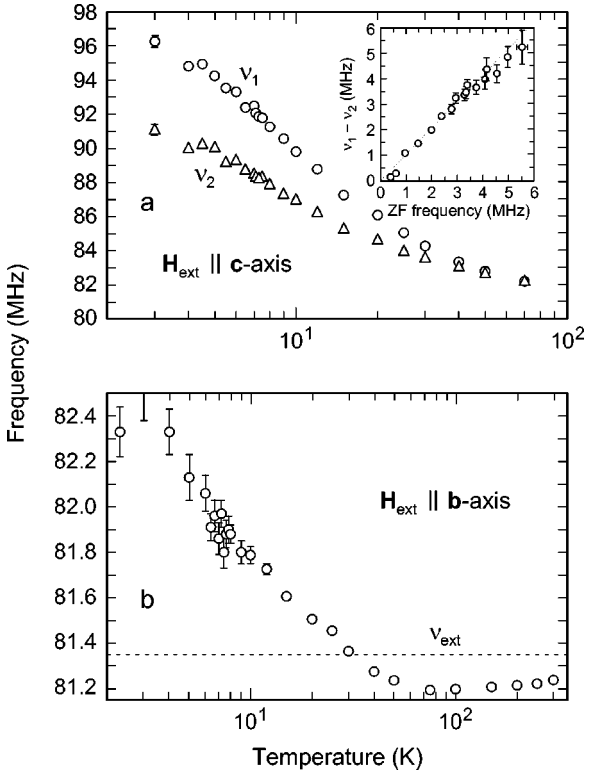

FIG. 18. (a) Temperature dependence of the precession frequencies $\omega_1/2\pi$ and $\omega_2/2\pi$ ($H_{ext}=6$ kOe). The inset shows $(\omega_1-\omega_2)/2\pi$ versus the spontaneous frequency in ZF. (b) Temperature dependence of $\omega_3/2\pi$. The frequency $\nu_{ext}=(\gamma_\mu/2\pi)H_{ext}$ is indicated by the horizontal dashed line.

$\omega_{ext}/2\pi$, arising in the presence of only H_{ext}, for $T>40$ K, signaling a negative Knight shift, and it changes to values above $\omega_{ext}/2\pi$ for $T<40$ K, signaling now a positive Knight shift. The Gaussian relaxation rates for all three orientations are presented in Fig. 19 together with the zero field σ for $\boldsymbol{P}_\mu \| \boldsymbol{b}$ axis. We note rather different behaviors. In particular, σ in TF for $\boldsymbol{H}_{ext} \| \boldsymbol{b}$ axis is clearly much smaller than in ZF. This is in part understandable given that $B_{tot}=\sqrt{H_{ext}^2+B^2}$ [Eq. (17)] and hence the variance in $B, \Delta B$, translates as follows into the variance of $B_{tot}, \Delta B_{tot}$:

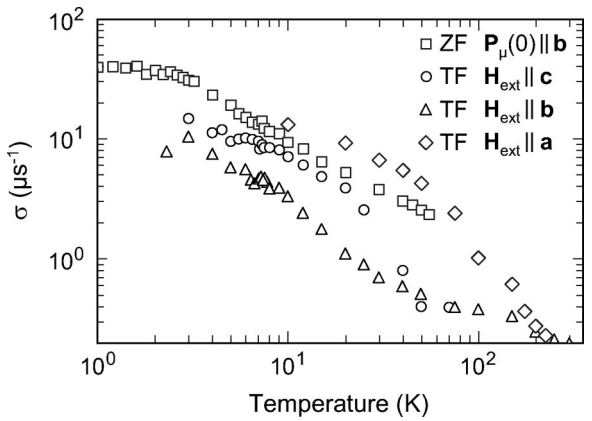

FIG. 19. Temperature dependence of the Gaussian relaxation rates σ in ZF and TF (6 kOe) for various orientations.

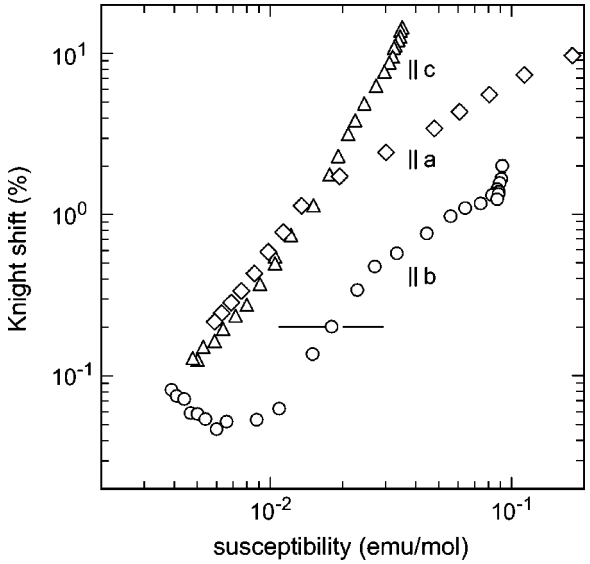

FIG. 20. Clogston-Jaccarino plot of the Knight shift for H_{ext} oriented along the a, b, and c axis versus the bulk susceptibility. K_b is shifted up by 0.2% to allow its display on a log scale. The horizontal line corresponds to $K_b=0$.

$$\Delta B_{tot}=\frac{\Delta B B}{\sqrt{B^2+H_{ext}^2}} \underset{H_{ext}\gg B}{\rightarrow} \frac{\Delta B}{H/B}. \tag{22}$$

For $\boldsymbol{H}_{ext} \| \boldsymbol{a}$ axis σ is much larger than for the other two orientations. This is, however, a consequence of not having performed a two-component fit.

The Knight shift is extracted from the (average) shift of the precession frequencies by correcting for the demagnetization and Lorentz fields and using for the bulk susceptibility data from Ref. 9. The demagnetization factors were estimated according to Ref. 17. In Fig. 20, we plot the Knight shifts, labeled K_a, K_b, K_c for the three orientations of $\boldsymbol{H}_{ext}$ versus the bulk susceptibility χ_{bulk}. Conventionally, the Knight shift is expected to scale with χ_{bulk} and the data in Fig. 20 should fall on straight lines. As is evident this is absolutely not the case. In particular, the behavior of K_b with a change of sign at ~ 40 K calls for a more sophisticated explanation.

B. Determination of the μ^+ site

We recall that the Knight shift consists of two contributions: the contact-hyperfine term and a dipolar field term. The dipolar field originates from the moments induced by the external field $\boldsymbol{H}_{ext}$, and the contact term arises from the spin polarization of the conduction electrons at the μ^+ site. The spin polarization is dominantly caused via the Ruderman-Kittel-Kasuya-Yosida (RKKY) mechanism by the moments induced in the $4f$ shell of Pr^{3+}. As usual we may write[16]

$$K_a=(A_0+A_{aa}^{dip})\chi_a+K_a^0, \tag{23a}$$

$$K_b=(A_0+A_{bb}^{dip})\chi_b+K_b^0, \tag{23b}$$

$$K_c=(A_0+A_{cc}^{dip})\chi_c+K_c^0, \tag{23c}$$

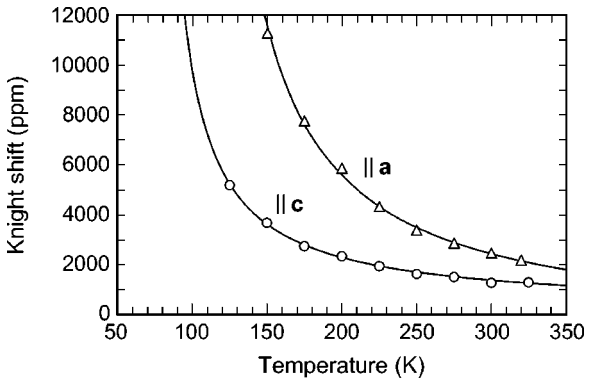

FIG. 21. Temperature dependence of K_a and K_c above 100 K. The solid lines represent Curie-Weiss fits [Eq. (24)].

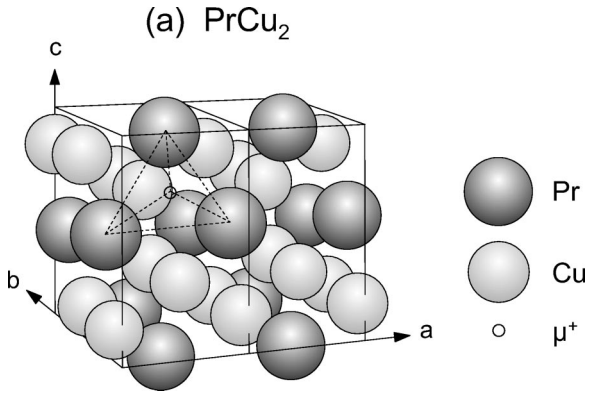

FIG. 22. Crystal structure of orthorhombic (space group *Imma*, No 74) $PrCu_2$ with the μ^+ site indicated.

where A_0 is the contact-coupling constant assumed to be isotropic and temperature independent, A_{ii}^{dip} are the diagonal elements of the dipolar coupling tensor $\vec{\vec{A}}_{dip}$ with $\Sigma A_{ii}^{dip}=0$, and χ_i are the components of a local susceptibility tensor $\vec{\vec{\chi}}_{loc}$ which characterizes the magnetic response of the Pr atoms in the neighborhood of μ^+. The absence of scaling in Fig. 20 indicates that $\vec{\vec{\chi}}_{loc}$ is different from $\vec{\vec{\chi}}_{bulk}$. This will in part be a μ^+-induced effect[18] (see below). The coupling tensor depends on the μ^+ location in the considered lattice and vice versa the determination of $\vec{\vec{A}}_{dip}$ allows us to identify the μ^+ site usually unambiguously.

The absence of scaling appears to render it impossible to extract A_{ii}^{dip} from $K_i(T)$. Fortunately we find that above 100 K, K_a and K_c show a perfect Curie-Weiss temperature dependence,

$$K_i=\frac{A_i C}{T-T_{C,i}}+K_i^0 \quad (i=a,c), \tag{24}$$

where K_i^0 are temperature-independent contributions. Corresponding fits are displayed in Fig. 21. Although the loss of scaling can be attributed to a μ^+-induced modification of the magnetic response of the nearest Pr neighbors, the ionic state of Pr, i.e., Pr^{3+}, cannot be changed. Hence the factor C can be identified with the Curie-Weiss constant $C=[N\cdot J(J+1)/3k_B]g_J^2\mu_B^2(=1.6$ K emu/mol for $Pr^{3+})$ and $A_i=A_0+A_{ii}^{dip}$. The fitted parameters A_i, K_i^0, and $T_{C,i}$ are collected in Table I. In other words, the modified susceptibility above 100 K follows a Curie-Weiss behavior, like the bulk susceptibility, but with very different Curie-Weiss temperatures (see Table I). Similar observations have been made before in $U_{14}Au_{51}$ (Ref. 18) and Ce_7Ni_3.[19]

TABLE I. Collection of fit parameters [Eq. (24)].

	$\boldsymbol{H}_{ext}\|\mathbf{a}$	$\boldsymbol{H}_{ext}\|\mathbf{c}$	$\boldsymbol{H}_{ext}\|\mathbf{b}$
A_i(kG/μ_B)	2.318 (3)	0.433 (3)	−1.122 fixed
K_{ii}^0 (ppm)	−836(24)	188 (32)	−515(20)
T_c (K)	96.4 (5)	71.8 (1.3)	−138 (8)
$T_{c,bulk}$ (K)	22.7	−32.7	−102 (1)
A_{ii}^{dip} (kG/μ_B)	1.609	0.222	−1.831
A_0 (kG/μ_B)	0.709	0.709	0.709

[a]See text.

Concerning K_b, the temperature dependence above 100 K is too weak to allow a precise determination of A_b in the same way as for K_a and K_c. This presents a problem because the determination of the four coupling constants $A_0, A_{aa}^{dip}, A_{bb}^{dip}$, and A_{cc}^{dip} requires knowledge of all three $A_i(i=a,b,c)$. Therefore we followed a different approach. From the fact that the precession signal shows no splitting, independent of orientation, follows that $\vec{\vec{A}}_{dip}$ possesses only diagonal elements. Calculations show that, except for the 4e sites [see Fig. 22], all other likely interstial sites, e.g., the $4d, 4c, 4b$ sites (Wyckoff notation) involve $\vec{\vec{A}}_{dip}$ with nonzero off-diagonal elements. Also, from an analysis of the spontaneous fields in the ordered state of $GdCu_2$ it was already known that μ^+ must reside at a site of the $4e$ type, e.g., at the position $(\frac{1}{2}\,\frac{1}{4}\,z)$ with $z=0.613$.[20] This is near the center of the triangles formed by three Pr atoms, see Fig. 22. Assuming that this site is also occupied by the μ^+ in $PrCu_2$, we compared $A_a-A_c=A_{aa}^{dip}-A_{cc}^{dip}=1.385(6)$ kG/μ_B with calculations[21] changing only the z value around the center position of the triangle.[22]

In Fig. 23, we plot the calculated $A_{aa}^{dip}-A_{cc}^{dip}$ versus z and include the measured value as a horizontal line (and error bars). From the intersection of the two lines, it follows that $z=0.6406\pm0.0004$. For this site we calculate $A_{aa}^{dip}=1.609$ kG/μ_B, $A_{bb}^{dip}=-1.831$ kG/μ_B, and $A_{cc}^{dip}=0.222$ kG/μ_B $(A_{i\neq j}^{dip}=0)$, which enables us now to determine also $A_0=A_a-A_{aa}^{dip}=0.709(3)$ kG/μ_B and $A_b=A_0+A_{bb}^{dip}=-1.122$ kG/μ_B. By fixing the latter value in Eq. (24) and fitting it to $K_b(T)$ for $T>100$ K also $T_{c,b}$ and K_{bb}^0 are determined (see Table I). The inset in Fig. 23 pictures the Pr triangle and the μ^+ position within. We see that the μ^+ is nearly equally spaced from the three Pr positions.

We briefly comment on the loss of scaling of K_i with χ_{bulk}. While above 100 K the change of the Curie-Weiss temperature can be explained as a muon-induced modification of the crystalline-electric-field splitting of the $^3H_4$ ground-state multiplet and possibly also of the exchange coupling of the three nearest Pr neighbors, the change of sign of K_b at ~40 K cannot arise from the local susceptibility.

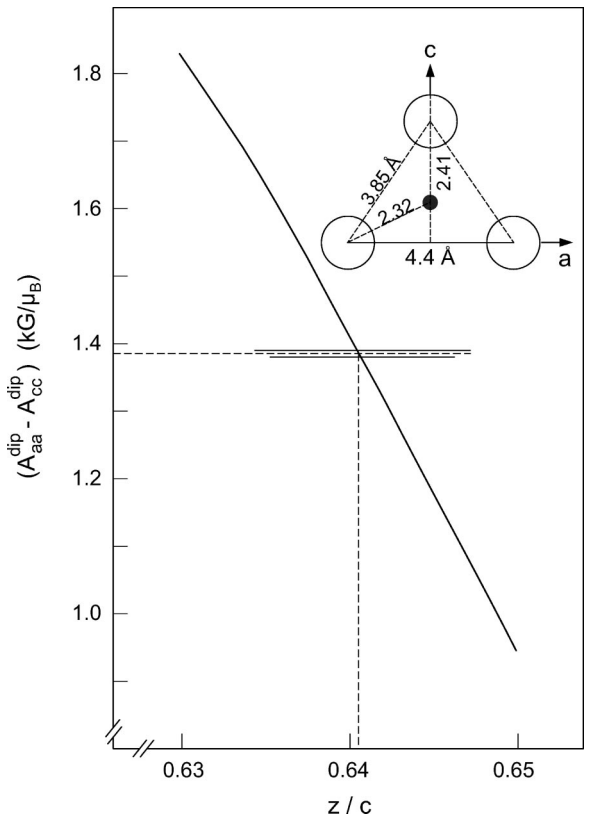

FIG. 23. Plot of calculated $A_{aa}^{dip}-A_{cc}^{dip}$ versus the z coordinate of the e site at $(\frac{1}{2},\frac{1}{4},z)$. The horizontal line represents the measured value leading to $z=0.6406$. The inset displays the position of μ^+ inside a Pr triangle.

Rather $A_b=A_0+A_{bb}^{dip}$ must exhibit the sign change. Since A_{bb}^{dip} is a temperature-independent parameter as long as no site change occurs, we have to conclude that A_0 becomes temperature dependent below ~ 100 K and, perhaps, also anisotropic. In any case this indicates that part of the temperature dependence of K_a, K_b, K_c below 100 K is connected to A_0. Since $A_{bb}^{dip}<0$, A_0 has to become larger with decreasing temperature. As to the possible mechanism leading to a temperature dependence of A_0 in the presence of quadrupolar degrees of freedom, we refer the reader to Ref. 23. Evidence for a temperature dependent A_0 has also been demonstrated in μSR studies of $U_{0.965}Th_{0.035}B_6$ (Ref. 24) and HoB_2C_2.[25]

V. DISCUSSION

A. Magnetic structure

As demonstrated above the ZF and LF measurements have revealed that the unexpected internal fields $\boldsymbol{B}$ below ~ 60 K are confined to the (a,c) plane and must show, on an average, a preferred direction close to the $[110]$ and $[1\bar{1}0]$ axes, respectively, the precise direction changing with temperature. The absolute value of $\boldsymbol{B}$ must also show a wide distribution, the width of which being of the same magnitude as the average. Can we understand this on the basis of some assumed magnetic structure?

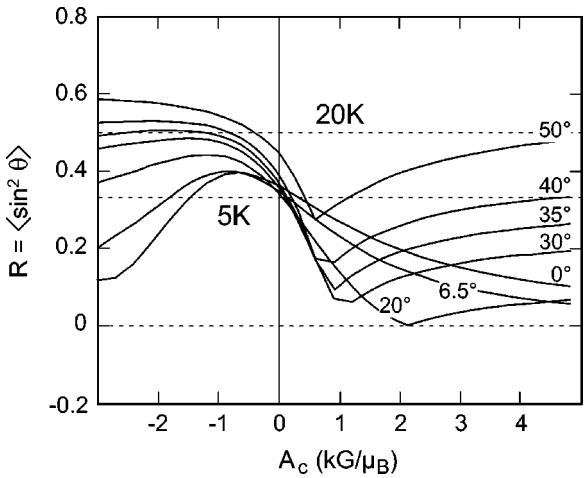

FIG. 24. Plot of calculated R [Eq. (32)] versus the contact-coupling constant A_0 for various angles ϱ. The indicated dashed horizontal lines represent the measured values at 5 K and 20 K.

Before we enter to deal with this question, and in anticipation of critical reactions, we consider the possibility that what we observe is somehow all muon induced. In our view the main objection against this possibility is the wide but nonisotropic scatter in the directions of $\boldsymbol{B}$ in the (a,c) plane (see below). Since μ^+ resides at a unique crystallographic site one would expect that a μ^+-induced effect is the same everywhere in the lattice. In addition both the appearance of a cutoff temperature in the temperature dependence of the zero-field precession frequency and the slowing down of the spin dynamics on approaching this temperature from above (albeit in a noncritical fashion) seem impossible to be explained as a μ^+-induced effect.

Returning to the question of the possible magnetic structure below 50 K, we start with the assumption that the modulated structure found below 60 mK may persist to high temperatures. Hence we assume that the ordered moment at position $\boldsymbol{R}_i$ is given by

$$\boldsymbol{\mu}(\boldsymbol{R}_i)=\boldsymbol{\mu}_0\cdot\cos(2\pi\boldsymbol{k}\cdot\boldsymbol{R}_i+\varphi) \tag{25}$$

and $\boldsymbol{\mu}_0=(\cos\varrho\,\hat{\boldsymbol{a}}+\sin\varrho\,\hat{\boldsymbol{c}})\mu_0$, where $\hat{\boldsymbol{a}}$ and $\hat{\boldsymbol{c}}$ are unit vectors along the a and c axes. According to Ref. 2, $\boldsymbol{k}=(0.24,0,0.68)$, $\varrho\simeq 6.5°$, and $\mu_0=0.54\mu_B$ for $T\to 0$ K. Since we have no detailed knowledge on the local magnetic structure within a Pr triangle and do not know the relative phases of the modulation within some generic triangle, we take that Eq. (25) is also describing the modulation of the moments within a triangle and set the overall phase $\varphi=0$.

The calculation of the dipolar field distribution over the μ^+ sites follows the procedures described in Ref. 16. Accordingly the field at a particular μ^+ site $\boldsymbol{R}_\mu$ can be expressed as

$$\boldsymbol{B}_{dip}(\boldsymbol{R}_\mu)=\boldsymbol{C}_{dip}\cdot\cos(2\pi\boldsymbol{k}\cdot\boldsymbol{R}_\mu)-\boldsymbol{S}_{dip}\cdot\sin 2\pi(\boldsymbol{k}\cdot\boldsymbol{R}_\mu) \tag{26}$$

with

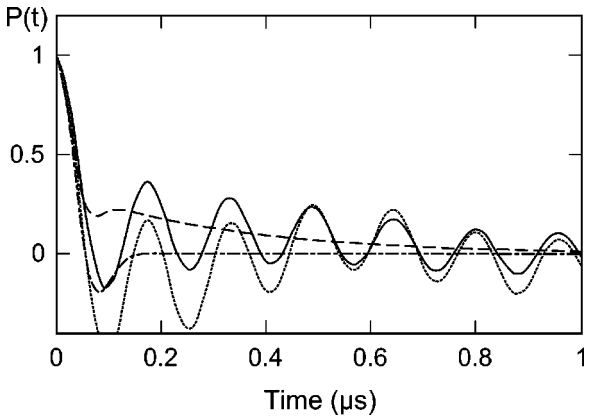

FIG. 25. Comparison of calculated and measured $P(t)$ at 5 K for $\boldsymbol{P}_\mu(0)\|\boldsymbol{c}$ axis (solid and dashed lines) and $\boldsymbol{P}_\mu(0)\|\boldsymbol{b}$ axis (dotted and dot-dashed lines). The experimental $P(t)$ is represented by the fitted Eq. (2).

$$\boldsymbol{C}_{dip}=\sum_i \left(\frac{3(\boldsymbol{\mu}_0\cdot\boldsymbol{r}_i)\boldsymbol{r}_i}{r_i^5}-\frac{\boldsymbol{\mu}_0}{r_i^3}\right)\cos(2\pi\boldsymbol{k}\cdot\boldsymbol{r}_i), \quad (27a)$$

$$\boldsymbol{S}_{dip}=\sum_i \left(\frac{3(\boldsymbol{\mu}_0\cdot\boldsymbol{r}_i)\boldsymbol{r}_i}{r_i^5}-\frac{\boldsymbol{\mu}_0}{r_i^3}\right)\sin(2\pi\boldsymbol{k}\cdot\boldsymbol{r}_i), \quad (27b)$$

where $\boldsymbol{R}_i$ denote the positions of the Pr ions and $\boldsymbol{r}_i=\boldsymbol{R}_i-\boldsymbol{R}_\mu$. The lattice sums are the same for all equivalent μ^+ positions. In $PrCu_2$, we find two magnetically inequivalent positions with the generic positions $(\frac{1}{2},\frac{1}{4},0.6406)$ and $(0,\frac{1}{4},0.8594)$. For both positions $\boldsymbol{C}$ is the same and $\boldsymbol{S}$ differs only by its sign. The lattice sums were extended over cubes of at least $10a\times10b\times10c$.[22] Because of the incommensurate $\boldsymbol{k}$ the argument $2\pi\boldsymbol{k}\cdot\boldsymbol{R}_\mu$ may be replaced in Eq. (26) by the continuous variable $\delta(0\leqslant\delta<2\pi)$ with each δ appearing with the same weight. The resulting spectral distribution of $|\boldsymbol{B}_{dip}|$ is identical for the two sites. In addition, we assume the presence of a contact-hyperfine field $\boldsymbol{B}_c(\boldsymbol{R}_\mu)$ induced by only the three Pr neighbors next to μ^+,

$$\boldsymbol{B}_c(\boldsymbol{R}_\mu)=A_0\sum_{i=1}^{3}\boldsymbol{\mu}(\boldsymbol{R}_\mu+\boldsymbol{r}_i)=A_0[\boldsymbol{C}_c\cdot\cos(2\pi\boldsymbol{k}\cdot\boldsymbol{R}_\mu)+\boldsymbol{S}_c\sin(2\pi\boldsymbol{k}\cdot\boldsymbol{R}_\mu)], \quad (28)$$

with

$$\boldsymbol{C}_c=\boldsymbol{\mu}_0\sum_{i=1}^{3}\cos(2\pi\boldsymbol{k}\cdot\boldsymbol{r}_i), \quad (29a)$$

$$\boldsymbol{S}_c=\boldsymbol{\mu}_0\sum_{i=1}^{3}\sin(2\pi\boldsymbol{k}\cdot\boldsymbol{r}_i). \quad (29b)$$

The total field at μ^+ is then given by $(2\pi\boldsymbol{k}\cdot\boldsymbol{R}_\mu=\delta)$

$$\boldsymbol{B}(\delta)=\boldsymbol{B}_{dip}(\delta)+\boldsymbol{B}_c(\delta)=(\boldsymbol{C}_{dip}+\boldsymbol{C}_c)\cos\delta+(\boldsymbol{S}_{dip}+\boldsymbol{S}_c)\sin\delta=\boldsymbol{C}\cos\delta+\boldsymbol{S}\sin\delta. \quad (30)$$

A_0 is the contact-coupling constant, assumed to be isotropic. The angle $\theta(\delta)$ between $\boldsymbol{B}(\delta)$ and the a axis, entering into Eqs. (9), (10), (12), and (13), follows from the relation (see Fig. 10)

$$\sin(\theta(\delta))=\frac{\boldsymbol{B}(\delta)\cdot\hat{\boldsymbol{c}}}{|\boldsymbol{B}(\delta)|}, \quad (31)$$

where, as before, $\hat{\boldsymbol{c}}$ is a unit vector along the c axis. In the experiment, we will see an average over all δ values $(0\leqslant\delta<2\pi)$ and the $\sin^2\theta$ factor in Eqs. (12a), (12b), and (13a), (13b) has to be replaced by

$$\sin^2\theta\rightarrow\frac{1}{2\pi}\int_0^{2\pi}\left(\frac{\boldsymbol{B}(\delta)\cdot\hat{\boldsymbol{c}}}{|\boldsymbol{B}(\delta)|}\right)^2 d\delta\equiv R, \quad (32)$$

and the $\sin2\theta$ factor in Eqs. (12c) and (13c) by a corresponding average.

The calculations show that R is the parameter that most sensitively depends on the assumed magnetic structure, e.g., on the angle ϱ and also on the contact-coupling constant A_0. In Fig. 24, we plot calculated R versus A_0 for different ϱ. Also indicated in this figure are the experimental values of R measured at 5 K and 20 K. We recognize that $R=0.5$ can only be reproduced if $A_0<0$ and $\varrho>30°$. $R\simeq0.33$ (the 5-K value) can be reproduced for all ϱ, but again A_0 will have to be <0.4 kG/μ_B or negative. This appears to contradict our earlier conclusion in Sec. IV that below 40 K, $A_0>|A_{bb}^{dip}|=1.83$ kG/μ_B. It seems that A_0 connected to field-induced moments behaves differently as compared with A_0 connected to the ordered moments in zero applied fields (ZF). We have no explanation for this behavior, but point out that the field shifts in the TF measurements at low T are much larger than the spontaneous fields seen in ZF. It is also interesting to note that the spontaneous fields, or the relevant ordered moments are not affected by the applied fields [see inset in Fig. 18(a)]. The calculations also show that $\int_0^{2\pi}\sin[2\theta(\delta)]d\delta=0$ for all A_0 in accordance with the absence of any signal in the right detector.

In a next step we assume that at low T, $\varrho=6.5°$ according to Ref. 2. Then (see Fig. 24) at 5 K, $A_0=-1.81$ kG/μ_B. Assuming that this value is the same at 20 K, we find $\varrho=34°$. The time evolution of the μ^+ polarization $P(t)$ in forward/backward direction can be calculated as follows. For $\boldsymbol{P}_\mu(0)\|\boldsymbol{b}$ axis

$$P(t)^{F/B}=\frac{1}{2\pi}\int_0^{2\pi}\cos[2\pi\gamma_\mu B(\delta)t]d\delta \quad (33)$$

and for $\boldsymbol{P}_\mu(0)\|\boldsymbol{c}$ axis, $\alpha=0$,

$$P(t)^{F/B}=\frac{1}{2\pi}\int_0^{2\pi}\{\cos^2[\theta(\delta)]\cos[2\pi\gamma_\mu B(\delta)t]+\sin^2[\theta(\delta)]e^{-\lambda t}\}d\delta. \quad (34)$$

λ has to be taken from the experimental results. In Fig. 25, we compare calculated $P(t)$ with experimental $P(t)$ at 5 K ($\lambda = 3.2\ \mu s^{-1}$). It is evident that the calculated $P(t)$ (the ordered moment is set to $\mu_0 = 0.175\mu_B$, see below) are much less damped than the experimental $P(t)$. This can also be seen from a calculation of the second moment of the spectral distribution of $|\boldsymbol{B}|$. The latter can be analytically expressed as (not normalized)

$$P(B) = \frac{2B}{\sqrt{[2B^2 - (\boldsymbol{C}^2 + \boldsymbol{S}^2)]} \cdot \sqrt{[\sqrt{(\boldsymbol{C}^2 - \boldsymbol{S}^2)^2 + 4(\boldsymbol{S}\cdot\boldsymbol{C})^2} + \boldsymbol{S}^2 + \boldsymbol{C}^2 - 2B^2]}}. \tag{35}$$

The second moment calculated for the 5-K case is $M_2 = 2 \times 10^3\ G^2$, which corresponds to a damping rate $\sigma = 3.8\ \mu s^{-1}$. The experimental values at 5 K are 19.2 μs^{-1} [$\boldsymbol{P}_\mu(0) \| \boldsymbol{b}$ axis] and 25 μs^{-1} [$\boldsymbol{P}_\mu(0) \| \boldsymbol{c}$ axis]. Apparently the field inhomogeneity is further enhanced by some different mechanism. Hence we multiply in Eqs. (33) and (34) the oscillating term with a Gaussian decay function, exp $(-\frac{1}{2}\sigma^2 t^2)$. Adjusting σ and μ_0 and keeping A_0 fixed to -1.81 kG/μ_B and ϱ to 6.5°, we arrive at a perfect fit of the 5-K data [see Fig. 26(a)] with $\mu_0 = 0.175\mu_B$, $\sigma[\boldsymbol{P}_\mu(0) \| \boldsymbol{b}$ axis$] = 15.7\ \mu s^{-1}$ and $\sigma[\boldsymbol{P}_\mu(0) \| \boldsymbol{c}$ axis$] = 23\ \mu s^{-1}$. The 20-K data are reproduced equally well with $\mu_0 = 0.058\mu_B$, $\varrho = 34°$, $\sigma[\boldsymbol{P}_\mu \| \boldsymbol{b}$ axis$] = 7.0\ \mu s^{-1}$, $\sigma[\boldsymbol{P}_\mu \| \boldsymbol{c}$ axis$] = 7.15\ \mu s^{-1}$, and A_0 kept at -1.81 kG/μ_B [Fig. 26(b)]. For completeness, Fig. 27 displays $\theta(\delta)$ and $B(\delta)$ pertaining to the 5-K case. Repeating the above procedure for the lowest temperature (0.02 K), we obtain $\mu_0 = 0.29\mu_B$ ($\varrho = 6.5°$, $A_0 = -1.81$ kG/μ_B). The LF data are also excellently reproduced on the basis of the derived values just quoted.

The LF signals are only observed in the forward/backward directions. Defining [see Eqs. (14)–(17)]

$$B_{tot,b}(\delta) = \sqrt{H_{ext}^2 + B(\delta)^2}, \tag{36}$$

$$B_{tot,c}(\delta) = \sqrt{H_{ext}^2 + B(\delta)^2 + 2H_{ext}B_c(\delta)}, \tag{37}$$

$$A_\omega(\delta)_b = 1 - \frac{H_{ext}^2}{B_{tot,b}(\delta)^2}, \tag{38}$$

$$A_\omega(\delta)_c = 1 - \frac{[\boldsymbol{H}_{ext} + \boldsymbol{B}_c(\delta)]^2}{B_{tot,c}(\delta)^2}, \tag{39}$$

$$B_c(\delta)_c = B(\delta)\sin[\theta(\delta)], \tag{40}$$

the average precession amplitudes and frequencies are given as follows. For $\boldsymbol{H}_{ext} \| \boldsymbol{b}$ axis,

$$\langle A_\omega \rangle_b = \frac{A}{2\pi}\int_0^{2\pi} A_\omega(\delta)_b d\delta, \tag{41}$$

$$\langle \nu \rangle_b = \frac{(\gamma_\mu/2\pi)A}{\langle A_\omega \rangle_b}\int_0^{2\pi} A_\omega(\delta)_b B_{tot,b}(\delta) d\delta \tag{42}$$

and, for $\boldsymbol{H}_{ext} \| \boldsymbol{c}$ axis,

$$\langle A_\omega \rangle_c = \frac{A}{2\pi}\int_0^{2\pi} A_\omega(\delta)_c d\delta, \tag{43}$$

$$\langle \nu \rangle_c = \frac{(\gamma_\mu/2\pi)A}{\langle A_\omega \rangle_c}\int_0^{2\pi} A_\omega(\delta)_c B_{tot,c}(\delta) d\delta. \tag{44}$$

As an example, the solid lines in Fig. 13 are calculated according to the above expressions using for μ_0, ϱ, A_0 the values estimated above for the 5-K case. However, in order to obtain good agreement with the data (in particular for ν) we had to take into account the enhancement of H_{ext} due to the Knight shift, demagnetization, and Lorentz fields in rough agreement with the TF results. Concerning the TF signals, they can be reproduced equally well, in particular the splitting can be traced back to the fact that H_{ext} ($= 6$ kOe) $\gg B$ in contrast to the LF measurements in smaller H_{ext}.

We return to the question of the origin of the enhanced field inhomogeneity in ZF relative to what is be expected from the incommensurate structure. One possible explanation is that it arises from the hyperfine-enhanced Pr nuclear-dipole fields. The bare Pr nuclei will produce a Gaussian shaped field distribution at the μ^+ sites[26] which leads to anisotropic damping constants of $\sigma_0 = 0.387\ \mu s^{-1}$ ($0.355\ \mu s^{-1}$) for $\boldsymbol{P}_\mu(0) \| \boldsymbol{b}$ axis and $\sigma_0 = 0.346\ \mu s^{-1}$ ($0.298 \mu s^{-1}$) for $\boldsymbol{P}_\mu(0) \| \boldsymbol{c}$ axis in the Van Vleck or quadrupolar limit (radial electric-field gradients assumed[26]), respectively. Comparing these values with the estimated σ we arrive, at 5 K, at enhancement factors $\eta = \sigma/\sigma_0$ ranging from 66 for $\boldsymbol{P}_\mu(0) \| \boldsymbol{c}$ axis to 40 for $\boldsymbol{P}_\mu(0) \| \boldsymbol{b}$ axis (in the Van Vleck limit). These values are about a factor of 2 larger than estimates presented in Refs. 1 and 4. Since the enhancement factor is proportional to the susceptibility of the Pr ions, it is reasonable that σ shows a $1/T$ dependence at higher temperatures [see inset in Fig. 8 and Eq. (4)]. The increased value of η may be due to a modification of the CEF splitting of the three Pr ions next to the μ^+ site. Another reason for the enhanced field inhomogeneity may arise from a highly distorted magnetic structure involving short correlation length. This may also explain the absence of magnetic Bragg peaks in neutron scattering above 50–60 mK.

Summarizing the discussion we can state that the observed internal field distribution is not inconsistent with the incommensurate structure derived from the neutron work. However, the amplitude of the modulation at the lowest T is

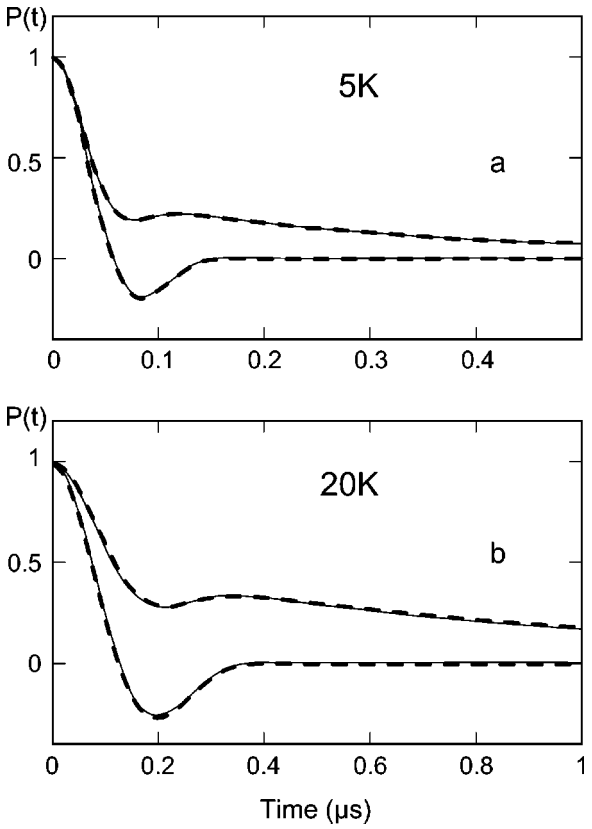

FIG. 26. Comparison of calculated and measured $P(t)$ at (a) 5 K and (b) 20 K. In contrast to Fig. 25, the calculated oscillating components in Eqs. (33) and (34) are damped by an additional Gaussian decay factor. Note the perfect agreement between data (bold dashed lines) and calculations (thin solid lines) (see text).

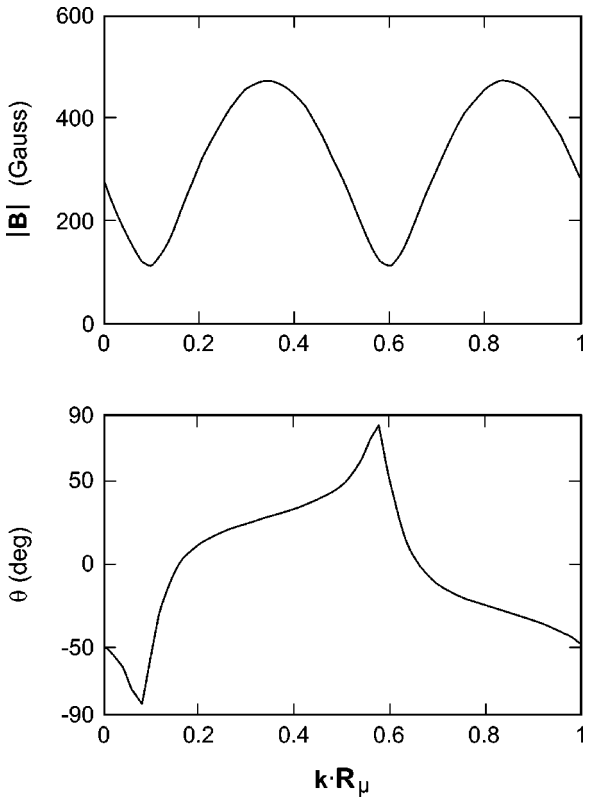

FIG. 27. Plot of (a) $|\boldsymbol{B}|$ and (b) θ versus $\delta=\boldsymbol{k}\cdot\boldsymbol{R}_{\mu}$ pertaining to the 5-K case ($\varrho=6.3°$, $A_0=-1.81$ kG/μ_B, $\mu_0=0.175\mu_B$).

of the order of $0.29\mu_B$, i.e., smaller by almost a factor of 2 compared with the quoted value in Ref. 2. In addition, the contact-coupling constant associated with the ordered moments is different from what is expected on the basis of the Knight-shift results. Independently of the magnetic structure adopted in our analysis, our data imply that the average orientation of the ordered moments rotates from being nearly parallel to the a axis at low T towards the $[101]$ direction in the (a,c) plane at 20 K. We can also state that the observed magnetic structure does not seem to be affected by the application of an external field up to 6 kOe.

B. Spin dynamics

Another puzzling aspect of the μSR results is the coexistence of static order and strong dynamically fluctuating field components. The latter phenomenon is characterized by a seemingly complex temperature dependence [see Fig. 14]. The field dependence of λ was shown in Sec. III E to follow Eq. (19). The first term of this equation is of the form of the Redfield formula[27]

$$\lambda_{Re}=\frac{1}{T_1}=(\gamma_{\mu}\tilde{B}_{\perp})^2\frac{\tau_c}{1+\omega^2\tau_c^2}, \tag{45}$$

where $\tilde{B}_{\perp}$ is the (average) amplitude of the fluctuating field component perpendicular to the total static field at μ^+. In the Redfield formula, ω is the μ^+ Zeeman frequency which involves the total static field at μ^+ [see Eqs. (36) and (37)]. However, it proved impossible to obtain satisfying fits if $\omega=\gamma_{\mu}B_{tot}$ is used in Eq. (45), instead the fits indicate that $\omega=\gamma_{\mu}H_{ext}$. On the other hand, we may assume that $\omega\tau_c\ll 1$ and ascribe the field dependence to the correlation time τ_c. However, this would lead to unphysically large values for $\tilde{B}_{\perp}$. In order to understand this puzzling situation, it is helpful to recall that quite generally $1/T_1$ is given by the Fourier transform of the local field correlation function evaluated at the μ^+ Zeeman frequency.[27] Equation (45) is obtained when one assumes that the correlation function follows a simple exponential decay. However, the correlation function may be more complicated, e.g., showing also an oscillating time dependence in addition to the exponential behavior. By proper modeling of the correlation function, it is in principle possible to arrive, at least approximately, at Eq. (45) with $\omega\simeq\gamma_{\mu}H_{ext}$. Hence, without trying to be more explicit, we will continue to view the fitted τ_c and $\tilde{B}_{\perp}$ as the relevant correlation times and fluctuating field amplitudes, respectively. A proper fit of $\lambda(H_{ext})$ required also a second field-independent term λ_{con} [see Eq. (19)]. The fit results for τ_c, $(\gamma_{\mu}\tilde{B}_{\perp})^2$ and λ_{con} at various temperatures are displayed in Fig. 28. The correlation time τ_c increases from $\sim 10^{-8}$ s at 2 K to a maximum of $\sim 3\times 10^{-7}$ s at 50 K followed by a decrease for $T>50$ K. Curiously the details in the temperature region around the maximum depend on the orientation

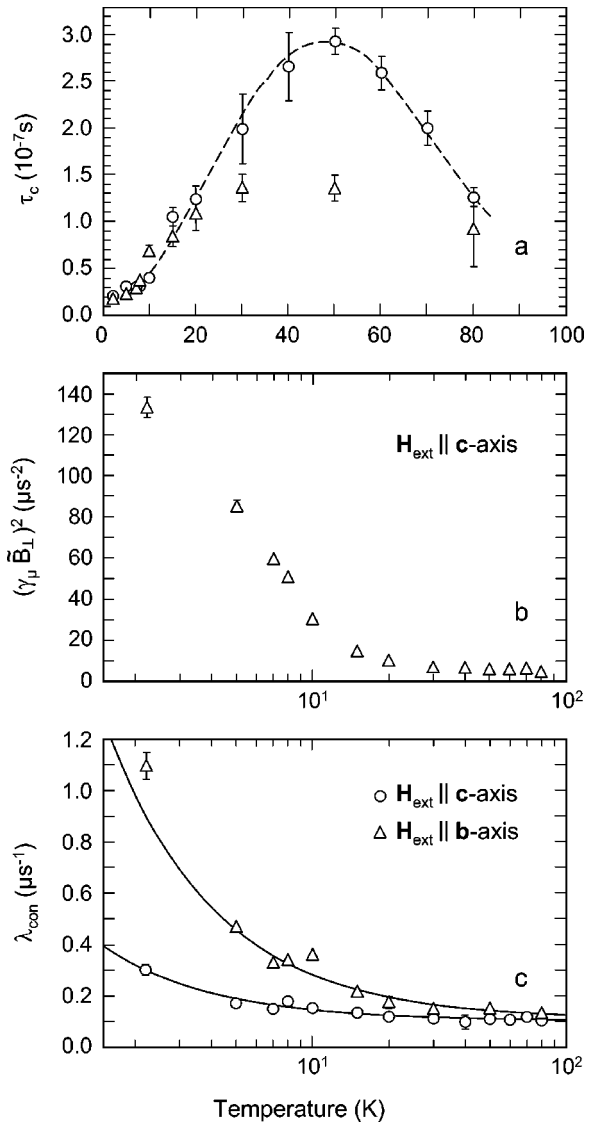

FIG. 28. Temperature dependence of (a) τ_c, (b) $(\gamma_\mu \tilde{B}_\perp)^2$, and (c) λ_{con}. The solid lines in (c) represent fits of Eq. (18).

of $\boldsymbol{H}_{ext}$. Below 20 K and above 80 K, τ_c appears to be isotropic. $(\gamma_\mu \tilde{B}_\perp)^2$ shows a fast decline with temperature and becomes temperature independent for $T \geqslant 30$ K. No significant anisotropy is seen (the data for $\boldsymbol{H}_{ext} \| \boldsymbol{b}$ axis are not shown for clarity). At 2 K, $\tilde{B}_\perp \simeq 135$ G and at 30 K, $B_\perp \simeq 31$ G. The corresponding static fields are 456 G and 70 G, respectively.

The constant term λ_{con}, on the other hand, shows a pronounced anisotropy and an overall temperature dependence like the 2-kOe data in Fig. 15(b), i.e., $\lambda_{con} \propto 1/T$. The anisotropy implies that the fluctuating fields are confined to the (a,c) plane. If within the (a,c) plane the fluctuating fields are randomly oriented, one would expect $\lambda_{con}(\boldsymbol{H}_{ext} \| \boldsymbol{b})/\lambda_{con}(\boldsymbol{H}_{ext} \| \boldsymbol{c}) = (\tilde{B}_\perp)^2/0.5(\tilde{B}_\perp)^2 = 2$. At 2.2 K we find $\lambda_{con}(\boldsymbol{H}_{ext} \| \boldsymbol{b})/\lambda_{con}(\boldsymbol{H}_{ext} \| \boldsymbol{c}) \cong 3.67$, indicating that $\tilde{B}_\perp$ is not randomly oriented. Labeling the relevant correlation time $\tau_{c,2}$, we now have the condition $\omega \tau_{c,2} \ll 1$, and $\lambda_{con} \propto \tau_{c,2} \propto 1/T$. Hence the fluctuation rate $\nu = 1/\tau_{c,2}$ appears to be of the Korringa type. It is reasonable to consider the fluctuation rate ν to be the relaxation rate of a part of the Pr $4f$ spin, confined, as its static part, to the (a,c) plane and driven by some Korringa-type mechanism. We propose that the related relaxation of μ^+ involves fluctuating electronic dipole fields, while the fluctuating (isotropic) contact-hyperfine fields are responsible for the field-dependent term of λ. The anomalous behaviors of τ_c and $(\gamma_\mu \tilde{B}_\perp)^2$ are then to be traced back to the RKKY mechanism, coupling the conduction electrons and the Pr $4f$ electrons. We suggest that the RKKY coupling constant is affected by the quadrupolar degrees of freedom of Pr^{3+}, changing the overlap integral with the conduction electrons[23] and rendering also the relevant contact-coupling constant $\tilde{A}_0$ time dependent due to stochastic rotational motion of the quadrupole moment. Hence $1/\tau_c$ is not necessarily connected to the behavior of magnetic dipoles but to that of higher multipole moments. In any case, τ_c would characterize the fluctuations of the contact-hyperfine field at μ^+. The decrease of $\tilde{B}_\perp^2$ could be explained as due to a decrease of the average $\tilde{A}_0^2$. The static A_0 and the dynamic $\tilde{A}_0$ are not necessarily tracking each other.

A further distinction between the field-dependent and field-independent terms of λ can be made: $\lambda(T)_{con}$ does not track the loss of the static spontaneous fields at ~ 65 K, but the Jahn-Teller transition at ~ 7.5 K, the latter is most pronounced at 4 kOe, the maximum field applied. The cusplike increase of λ_{con} at ~ 7.5 K signals an increase of $\tau_{c,2}$ which may be attributed to a slight slowing down of the Pr $4f$ spin dynamics. This is not seen in ZF, probably because λ_{con} is masked by the field-dependent term in Eq. (19), $\lambda(H)$. On the other hand, $\lambda(H)$ seems to be closely associated with the spontaneous order developing below ~ 65 K. Above 65 K it reflects the slowing down of fluctuating (contact hyperfine) fields, and below 65 K it is the dominant contribution to λ in zero and small LF. See also the remarks in the following section. Other scenarios might be envisioned as well. We leave it at that and just emphasize once more that the μ^+ relaxation behavior originates from two distinct and coexisting mechanisms. This has to be understood in future work.

C. Temperature dependence of ν_{ZF}

As we have seen in Sec. III B, the spontaneous frequency or field, respectively, follows a most unusual temperature dependence [Eq. (3)] which seems to be made up of two factors. The factor $(1-T/T_{cr})^\beta$ appears to reflect the order parameter and the other factor $[1-\exp(-E/kT)]$, some additional suppression of the spontaneous field. We have compared these factors with the temperature dependence of other parameters of $PrCu_2$. We found that the temperature dependence of the elastic constant C_{66} (Ref. 11) is precisely reproduced by $[1-\exp(-E/kT)]$ with $E = 5.15$ K. This is shown in Fig. 29. The stars are calculated according to

$$C_{66}(T) = C_0 - A[1-\exp(-E/kT)]. \tag{46}$$

They seem to track the data even better than the solid line

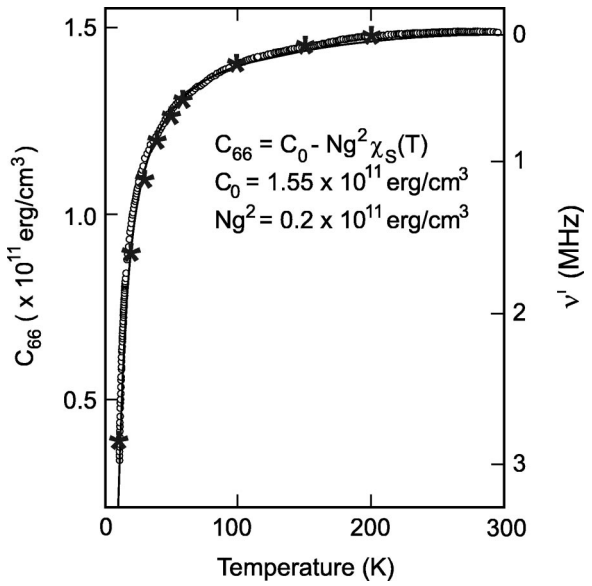

FIG. 29. Temperature dependence of the elastic constant C_{66}. The indicated stars are calculated with Eq. (46). The factor A is determined by normalizing Eq. (46) to $C_{66}(T)$ at 10 K.

which represents a calculation. According to Ref. 11, in second-order perturbation theory

$$C_{66}(T) - C_0 = -Ng^2\chi_{xy}(T), \tag{47}$$

where $\chi_{xy}(T)$ is the strain susceptibility, N is the number of ions per unit volume, and g is the magnetoelastic coupling constant. $\chi_{xy}(T)$ is given by

$$\chi_{xy}(T) = \sum_{n\neq m} \frac{2|\langle n|O_{xy}|m\rangle|^2}{E_n - E_m} + \frac{1}{kT}\left\{ \sum_n \frac{\exp(-E_n/kT)}{Z} |\langle n|O_{xy}|n\rangle|^2 - \left(\sum_n \frac{\exp(-E_n/kT)}{Z} \langle n|O_{xy}|n\rangle \right)^2 \right\}, \tag{48}$$

where $|n\rangle, |m\rangle$ are eigenstates of the CEF Hamiltonian acting on the Pr^{3+} ground-state multiplet $^3H_4$, E_n and E_m are the corresponding eigenvalues and $Z = \Sigma_n \exp(-E_n/kT)$ is the partition function. O_{xy} is the quadrupole moment (Stevens) operator. As was shown in Ref. 11 and mentioned in the Introduction, O_{xy} is also the relevant operator in the quadrupolar interaction responsible for the establishment of the ferroquadrupolar order below T_{JT}. Hence we may write for the ordered moment

$$\mu(T) = K\chi_{xy}(T)(1 - T/T_{cr})^{\beta}, \tag{49}$$

where K is some numerical constant. This empirical relation may lend itself to the following interpretation. The quadrupolar interaction causes strain which via the magnetoelastic coupling induces the complex magnetic order that we have seen. The strain itself disappears above T_{cr}. This would mean that below T_{cr} certain degrees of freedom of the quadrupole moments are frozen out, establishing a semiordered quadrupolar state, while the fully ferroquadrupolar state is only established below T_{JT}. This nonmagnetic origin could explain why the Pr^{3+} $4f$ moment dynamics is essentially unaffected by the onset of the order at ~65 K and why, on the other hand, the conduction-electron system provides a different channel of μ^+ relaxation via the stochastic time dependence of the contact-coupling constant.

Finally, we reiterate our suspicion that the phase transition at ~50 mK may concern only the Pr nuclear-spin system.

VI. SUMMARY AND CONCLUSIONS

The μSR measurements have established that some sort of magnetic order continues to exist in $PrCu_2$ up to T_{cr} ~65 K. The order appears to be consistent with what had been observed below 50 mK in neutron-scattering work,[2] but this may not be the only possible structure. In particular the modulated ordered moments are confined to the (a,c) plane, the angle between the ordered moment and the a axis changes from being close to zero at low temperatures to ~34° at 20 K. The amplitude of the modulation saturates at $0.27\mu_B$ below 1 K. The temperature dependence of the ordered moment is up to a factor $(1 - T/T_{cr})^{0.32}$ identical to the temperature dependence of the elastic constant C_{66},[11] which is proportional to the strain susceptibility.[11] This leads us to consider that the magnetic order is not of magnetic origin but induced by the strain arising from quadrupolar effects, which set in below T_{cr}. We do not see the phase transition at 50 mK. We propose that the phase transition seen in neutron scattering involves only the Pr nuclear-spin system.

Besides static spontaneous fields acting on μ^+, μ^+ is also subject to fluctuating fields, inducing relaxation of the μ^+ polarization component parallel to the total static field. It is found that the relaxation rate consists of a field-independent term and a field-dependent term, the latter following the Redfield formula. The field-independent term displays a $1/T$ dependence, while the field-dependent term involves unusual temperature dependencies of the correlation time and fluctuating field amplitude. We propose that the latter is caused by the contact-hyperfine field which acquires a stochastic time-dependence due to a time-dependent RKKY mechanism, which in turn is caused by the stochastic rotational motion of the $4f$ quadrupole moments. This presupposes that the involved overlap integral depends on the orientation of the quadrupole moment or the aspherical 4f electron charge distribution, respectively.[23] This stochastic rotational motion is slowed down and eventually partially frozen out when approaching T_{cr}.

We find that the total static field width monitored by μ^+ is much larger than what is expected from the modulated structure. We attribute this to random fields induced by the hyperfine enhanced Pr nuclear dipole fields involving an enhanced factor of order 60 at 5 K, about twice as large as estimated before.[1,4]

Transverse-field measurements served to determine the μ^+ site from the anisotropic Knight shift above 100 K. In agreement with earlier conclusions[3] and corresponding measurements in $GdCu_2$ (Ref. 20) and $CeCu_2$ (Ref. 28), we find the μ^+ to be located more or less at the center of a triangle

formed by three Pr ions in the (a,c) plane ($4e$ site). Above 10 K the μ^+ Knight shift follows, like the bulk susceptibility, a Curie-Weiss behavior but with very different Curie-Weiss temperatures. This must certainly be a μ^+-induced effect like it has been found in other rare-earth and U intermetallic compounds such as Ce_7Ni_3.[19] However, below 100 K we find evidence that the contact-hyperfine coupling constant becomes temperature and possibly also orientation dependent. This is attributed again to quadrupolar effects[23] and supports our idea that much of what has been seen in zero field is of quadrupolar interaction origin.

We like to mention that we have never seen in μSR measurements in other intermetallic compounds such a diversity of features as in $PrCu_2$. We now hope that theorists will feel challenged to understand these features in a quantitative manner.

ACKNOWLEDGMENTS

This work has been supported at various stages by Ch. Schmidlin, M. Pinkpank, A. Amato, and D. Andreica for which we are most grateful. We thank G. Solt (PSI) for illuminating discussions on theoretical aspects. Last but not least our thanks are also extended to the Laboratory for Muon-Spin Spectroscopy ($S\mu S$) and the accelerator crew of the Paul Scherrer Institut (PSI) for providing excellent measuring conditions.

[1] K. Andres, E. Bucher, J.P. Maita, and A.S. Cooper, Phys. Rev. Lett. **28**, 1652 (1972).
[2] S. Kawarazaki and J. Arthur, J. Phys. Soc. Jpn. **57**, 1077 (1988).
[3] A. Schenck, D. Andreica, F.N. Gygax, M. Pinkpank, Y. Onuki, P. Ahmet, M. Abliz, R. Settai, A. Amato, and N. Kaplan, Phys. Rev. B **58**, 5205 (1998).
[4] M. Wun and N.E. Phillips, Phys. Lett. **50A**, 195 (1974).
[5] H. R. Ott, K. Andres, P. S. Wang, Y. H. Wong, and B. Lüthi, *Crystal Field Effects in Metals and Alloys* (Plenum, New York, 1977).
[6] J.K. Kjems, H.R. Ott, S.M. Shapiro, and K. Andres, J. Phys. (Paris), Colloq. **39**, C6 (1978).
[7] K. Sugiyama, P. Ahmet, M. Abliz, H. Azuma, T. Takeuchi, K. Kindo, H. Sugawara, K. Motoki, H. Ikezawa, T. Ebihara, R. Settai, and Y. Onuki, Physica B **211**, 145 (1995).
[8] M. Abliz, R. Settai, P. Ahmet, D. Aoki, K. Sugiyama, and Y. Onuki, Philos. Mag. B **75**, 443 (1997).
[9] P. Ahmet, M. Abliz, R. Settai, K. Sugiyama, Y. Onuki, T. Takeuchi, K. Kindo, and S. Takayanagi, J. Phys. Soc. Jpn. **65**, 1077 (1996).
[10] T. Takuechi, P. Ahmet, M. Abliz, R. Settai, and Y. Onuki, J. Phys. Soc. Jpn. **65**, 1404 (1996).
[11] R. Settai, S. Araki, P. Ahmet, M. Abliz, K. Sugiyama, Y. Onuki, T. Goto, H. Mitamura, and T. Goto, J. Phys. Soc. Jpn. **67**, 636 (1998).
[12] J. K. Kjems, in *Electron Phonon Interactions and Phase Transitions*, edited by T. Riste (Plenum New York, 1977), p. 302.
[13] see, e.g., A. Schenck and F. N. Gygax, in *Handbook of Magnetic Materials*, edited by K. H. J. Buschow (Elsevier, Amsterdam, 1995), Vol. 9.
[14] A. Schenck, D. Andreica, F.N. Gygax, D. Aoki, and Y. Onuki, Phys. Rev. B **66**, 144404 (2002).
[15] A.B. Denison, H. Graf, W. Kündig, and P.F. Meier, Helv. Phys. Acta **52**, 460 (1979).
[16] See, e.g., A. Schenck, in *Muon Science*, edited by C. L. Lee, S. H. Kilcoyne, and R. Cywinski (IOP, Bristol and Philadelphia, 1998).
[17] P.G. Akishin and I.A. Gaganov, J. Magn. Magn. Mater. **110**, 175 (1992).
[18] A. Schenck, M. Pinkpank, F.N. Gygax, K.-U. Neumann, K.R.A. Ziebeck, and A. Amato, J. Phys.: Condens. Matter **10**, 8059 (1998).
[19] A. Schenck, D. Andreica, F.N. Gygax, K. Umeo, T. Takabatake, E. Schreier, A. Kratzer, and G.M. Kalvius, J. Phys.: Condens. Matter **13**, 4277 (2001).
[20] F.N. Gygax, D. Andreica, A. Schenck, M. Pinkpank, and Y. Onuki, J. Magn. Magn. Mater. **246**, 101 (2002).
[21] For the calculations of $\vec{A}_{dip}$ we used a computer program developed by A. Amato. Up to 10 shells of Pr atoms around the μ^+ site were included in the lattice sum calculations.
[22] The following lattice parameters were used in the calculation: $a = 4.40$ Å, $b = 7.024$ Å, $c = 7.435$ Å. The generic Pr Position is taken to be $(0, \frac{1}{4} 0.5377)$. A.R. Storm and K.E. Benson, Acta Crystallogr. **16**, 701 (1963).
[23] A. Schenck, F.N. Gygax, and K.A. McEwen, J. Phys.: Condens. Matter **14**, 4595 (2002).
[24] J.E. Sonier, R.H. Heffner, D.E. MacLaughlin, G.J. Niewnhuys, O. Bernal, R. Movshovich, P.G. Pagliuso, J. Cooley, J.L. Smith, and J.D. Thompson, Phys. Rev. Lett. **85**, 2821 (2000).
[25] F. De Lorenzi, F.N. Gygax, A. Schenck, A. Tobo, and H. Onodera, Physica B **326**, 581 (2003).
[26] see, e.g., A. Schenck, *Muon Spin rotation Spectroscopy* (Adam Hilger, Bristol, 1985).
[27] C. P. Slichter, *Principles of Magnetic Resonance* (Springer, Berlin, 1978).
[28] F. N. Gygax *et al.* (unpublished).
[29] See the homepage of the Laboratory for Muon Spin Spectroscopy of PSI, http://lmu.web.psi.ch